GEORG-AUGUST-UNIVERSITÄT
GÖTTINGEN

Fakultät für
Physik

Master's Thesis

Suche nach resonanter und nicht-resonanter Doppelhiggsproduktion im Zerfallskanal $\gamma\gamma WW^*$ bei hadronisch zerfallenden W-bosonen in geboosteter Topologie

Search for resonant and non-resonant di-Higgs production in the decay channel $\gamma\gamma WW^*$, with hadronically decaying W-bosons in boosted topology

prepared by

Kai Henßen

from Hannover

at the II. Physikalisches Institut

Thesis number:	II.Physik-UniGö-MSc-2017/02
Thesis period:	27th October 2016 until 31st March 2017
First referee:	Prof. Dr. Stan Lai
Second referee:	Prof. Dr. Arnulf Quadt

Abstract

A search for non-resonant and resonant di-Higgs production in the final state $hh \rightarrow \gamma\gamma WW^*$ with hadronically decaying W-bosons is performed. The analysis is based on 36.5 fb^{-1} of collision data recorded by the ATLAS experiment at the Large Hadron Collider in 2015 and 2016 at a center-of-mass energy of 13 TeV. The final state $\gamma\gamma W_{had}W^*_{had}$ combines the purity of $h \rightarrow \gamma\gamma$ with the relatively high branching ratio of $h \rightarrow WW^* \rightarrow qqqq$. The analysis was optimized for boosted topologies, where the quarks in the final state can be reconstructed by at least one large radius jet (Anti-$k_t(R = 1.0)$). The search is performed utilizing a cut and count approach, with Monte Carlo simulations representing non-resonant di-Higgs production and a spectrum of heavy resonances from 260 GeV to 3 TeV. The background composition is determined by a data-driven estimation in the $m_{\gamma\gamma}$ sidebands and Monte Carlo simulations of Standard Model $h \rightarrow \gamma\gamma$ processes.

No evidence of di-Higgs production is observed. Observed and expected upper exclusion limits at 95% confidence level on the production cross sections are set: The upper limits for the non-resonant production are at 6.36 pb (observed) and 8.26 $^{+4.07}_{-2.49}$ pb (expected). The upper limits for the resonant production are in the mass range of the resonance 1 TeV $\leq m_X \leq$ 3 TeV between 1.23 and 3.28 pb (observed) and between 1.75 and 4.70 pb (expected).

Keywords: Resonant di-Higgs production, Non-resonant di-Higgs production, Large radius jets, Physics, Master's thesis

Contents

1. Introduction

The study of subatomic particles is an important aspect of contemporary physics. The Standard Model of particle physics (SM) [1] is one of the most successful models to date [2–5]; it describes the existence of particles and interactions between them. Following theoretical considerations one of those particles was postulated in 1964 [6, 7] and recently discovered in 2012 [8, 9]: the Higgs-boson. However, several characteristics of this boson have not yet been experimentally tested. Furthermore, several theories predict the existence of more than one Higgs-boson. Investigations concerning the Higgs-sector and the underlying mechanism of spontaneous symmetry breaking are still a prominent facet of the experimental program of the ATLAS detector [10] and the LHC physics program.

This thesis will briefly describe the Standard Model of particle physics and its limitations, discuss the theoretical background of the Brout-Englert-Higgs (BEH) mechanism and beyond the Standard Model (BSM) models, which predict two Higgs doublets (2HDM) and consequently five Higgs-bosons [11]. These theories can address several of the SMs limitations. In particular, investigating di-Higgs processes allows for analysis of trilinear Higgs-couplings, which are sensitive to BSM contributions, as well as enables searches for heavy scalar BSM resonances.

Here, a search for di-Higgs production in the decay channel $hh \to \gamma\gamma WW^*$ with hadronically decaying W-bosons is presented. A particular focus lies on heavy resonances with masses above 1 TeV and the utilization of large radius jets.

This thesis is structured as follows: The theoretical background, including a description of the SM and its limitations, the BEH mechanism, 2HDMs and di-Higgs production is presented in chapter 2. The experimental apparatus (ATLAS) and methods of the analysis are described in chapter 3, while the event topology, reconstruction of objects, selection optimization and event yields are laid out in chapter 4. Chapter 5 presents the final results of the analysis, and chapter 6 provides a conclusion and outlines further prospects on the investigation of di-Higgs events. This thesis uses natural units: $c = \hbar = 1$.

2. Theoretical background

The Standard Model of particle physics (SM) [2–5], describes three of the four known fundamental forces (weak force, strong force and electromagnetic force) and all known fundamental particles. Despite the fact that many of its predictions agree with measured quantities to a very high precision [1], there are several shortcomings of the SM, that are of particular interest to this thesis. This chapter will describe some central ideas of the SM (sec. 2.1) with a particular focus on the Higgs sector (sec. 2.1.1 and 2.1.2) and for this analysis particularly relevant aspects like the decay of W-bosons. Furthermore, it will discuss limitations of the SM (sec. 2.1.3) and a Beyond-the-Standard-Model theory addressing some of those limitations by expanding the Higgs sector (sec. 2.2). Lastly searches for di-Higgs production are mentioned and discussed (sec. 2.3).

2.1. The Standard Model of particle physics

The SM is a gauge theory of the group $SU(3)_C \times SU(2)_L \times U(1)_Y$ that requires its Lagrangian density to be invariant under local gauge transformations. This requirement introduces gauge fields corresponding to massless force-carrying gauge bosons. These bosons correspond to different subgroups: Eight gluons couple to the color charge, C, (corresponding to the subgroup $SU(3)_C$) and mediate the strong nuclear force, while the fields for the subgroup $SU(2)_L \times U(1)_Y$ correspond to the mediators of the electroweak sector: $W^{\pm}$,Z^0,γ. This sector is the unification of the electromagnetic force and the weak force. In addition to these bosons, which are all spin-1 particles, the SM describes the spin-1/2 particles (fermions). Those fermions are the fundamental building blocks of matter in the universe and are subdivided into the leptons and the quarks, whereby only the latter carry color charge and are therefore subject to the strong interaction. Compound states of quarks are called hadrons. The fundamental particles, their charges, spins and masses are depicted in figure 2.1.

Most of the known fundamental particles have a finite lifetime and decay into lighter particles. Exceptions are the lightest particles as for them further decays are kinematically forbidden: Electrons and neutrinos are stable (ignoring neutrino oscillations, which only

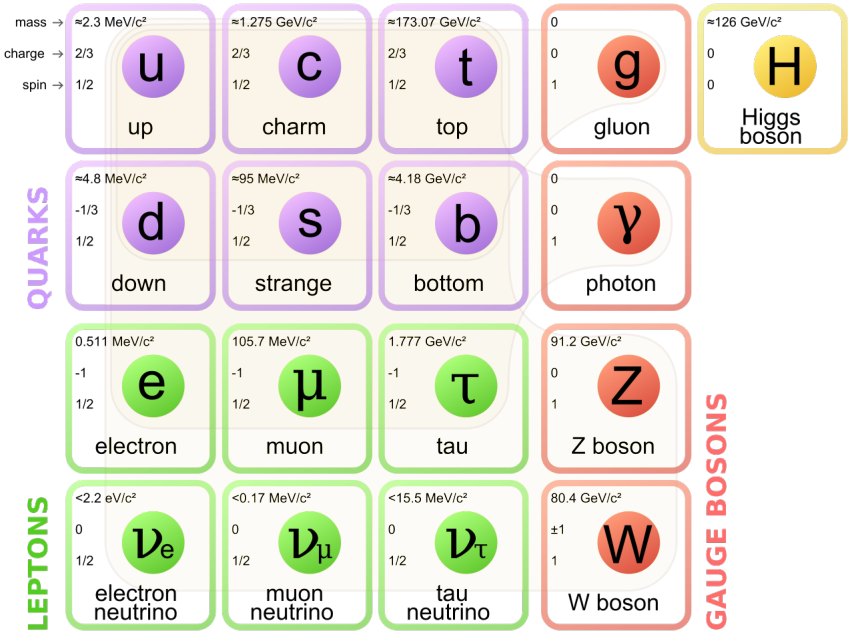

Figure 2.1.: Particle content of the SM showing fermions (leptons and quarks) and bosons (gauge bosons and the Higgs-boson). The gauge bosons are the photon, the gluon and the two vector bosons: W- and Z-boson. The particular groups of fermions and the gauge bosons they couple to are connected by a slightly shaded area (picture from [12])

.

change the neutrino flavor) as well as the lightest quarks (up, u and down, d), which form compound states. The other quarks decay according to the Cabbibo-Kobayashi-Maskawa (CKM) Matrix [13, 14] into a lighter quark and one of the W-bosons (such that electromagnetic charge is conserved). The CKM Matrix is related to the corresponding branching ratio (BR) for a given decay. The heavier leptons (μ and τ) decay into a corresponding (anti-)neutrino and a W-boson. This charged weak current is according to the SM the only process which results directly in flavor changes.

The weak nuclear force, of which the W-boson is one of the mediators, conserves electromagnetic charge, as well as spin and lepton or baryon number. Therefore a W-boson only decays into particle-antiparticle pairs, whose combined charge is equal to its own charge. Those particle-antiparticle pairs can be both quarks (with the exception of the top quark, as it is heavier than the W-boson) or leptons. In the hadronic decay only pairs of one up-type and one down-type quark, while in the leptonic decay only a charged lepton and the corresponding neutrino, are produced. Table 2.1 shows the branching ratios, while figure 2.2 depicts vertices of a W-boson decay.

Quarks, the decay products of hadronically decaying W-bosons, are, as well as the gluons, color confined i.e. combine to color singlets. If a parton (quark or gluon) has

Table 2.1.: Branching ratios of the W-boson [1].

Decay products	Branching Ratio [%]
hadrons	67.41 ± 0.27
$e\nu$	10.71 ± 0.16
$\mu\nu$	10.63 ± 0.15
$\tau\nu$	11.38 ± 0.27

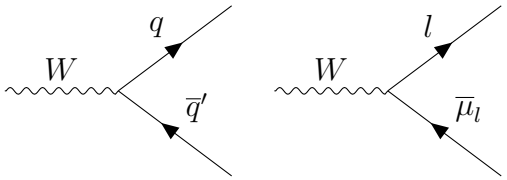

Figure 2.2.: Hadronic and leptonic W-boson decay.

sufficient energy, it can temporarily escape the singlet state and undergo so called parton showering: A cascade of partons is produced. These partons later combine again to color singlets and hadronize, forming hadrons. An explanation on how to combine information on the spray of hadrons and reconstruct a proxy for the initial parton, called a jet, is given in chapter 3.4.

2.1.1. The Brout-Englert-Higgs mechanism

At the heart of the SM lies the Brout-Englert-Higgs (BEH) mechanism [6, 7], it addresses two issues in the SM:

As a result of the local gauge invariance of the Standard Model, gauge fields were introduced, which require massless gauge bosons - a mass term in the Lagrange density for gauge bosons would violate local gauge symmetry. Experiments, however, showed that the W- and Z-bosons are massive.

In addition, WW scattering processes would *prima facie* violate unitarity at the TeV scale. This violation can be avoided if the scattering is mediated by a scalar particle, which possesses a coupling to WW proportional to m_W.

To address these issues, the Brout-Englert-Higgs mechanism was proposed, assuming the existence of a complex scalar field. The idea is to introduce a potential of this scalar field with a spontaneously broken symmetry, therefore creating a non-zero expectation value, see as an illustration figure 2.3.

Supposing the existence of a doublet, Φ, of complex scalar fields, Φ_1 and Φ_2, and arranging it such that Φ_2 is along the real axis, one can expand the doublet around the vacuum expectation value, v, introducing the scalar field, h:

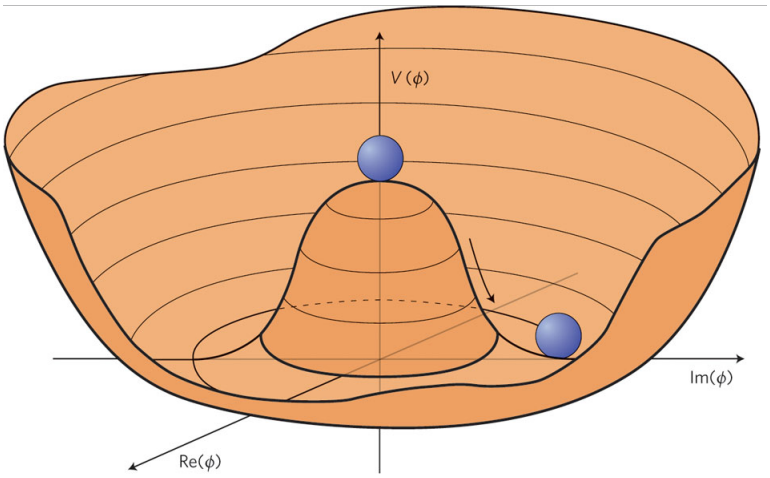

Figure 2.3.: Higgs potential and vacuum expectation value, v [15]. The minimum of the potential is no longer at the origin but a continuum. To reach the minimum, the symmetry must be spontaneously broken.

$$\Phi = \frac{1}{\sqrt{2}} \begin{pmatrix} 0 \\ v + h \end{pmatrix}.$$

In unitary gauge, the potential in $SU(2)$ can be written as:

$$V(\Phi) = \mu^2 \Phi^* \Phi + \eta (\Phi^* \Phi)^2,$$

such that for $\mu^2 < 0$ and $\eta > 0$ a stable (i.e. $\lim_{|\Phi| \to \infty} V(\Phi) = \infty$) symmetry is achieved, which can be spontaneously broken (i.e. minima exist, which are not at the axis of symmetry, as depicted in Figure 2.3).

The potential yields - after expansion around the local minimum - the following terms containing a new scalar boson, h:

$$\frac{1}{2} m_h^2 h^2 + \sqrt{\frac{\eta}{2}} m_h h^3 + \frac{\eta}{4} h^4.$$

This newly introduced scalar boson, called the Higgs-boson, has a mass of $m_h = \eta v^2/2$ and has trilinear and quartic self interactions. Introducing the new field yields mass-like terms in the Lagrange density for the vector bosons, which do not violate local gauge invariance. With the coupling constant g, the masses of the vector bosons are:

$$m_W = \frac{vg}{2}$$

and

$$m_Z = \frac{m_W}{\cos(\theta_W)},$$

where θ_W is the Weinberg angle. The coupling strength to a particle of the Higgs field is proportional to the particle's mass: In case of $W^{\pm}$ with an additional factor of g, in case of Z^0 with a factor of $g/\cos(\theta_W)$. For a fermion, f, the coupling strength, λ, to the Higgs field is $\lambda_f = \frac{\sqrt{2}m_f}{v}$.

2.1.2. The Standard Model Higgs-boson

In 2012, a Higgs-like particle with as a mass of approximately (125.09 ± 0.32) GeV [1] was discovered at the LHC experiments ATLAS and CMS [8, 9]. Production modes and cross sections for hadron colliders are shown in figure 2.4. At $\sqrt{s} = 13$ TeV, gluon-gluon fusion is the dominant process.

Some predicted branching ratios for a SM-like Higgs-boson are listed in table 2.2. Note that, the $\gamma\gamma$ final state cannot be produced at tree level, as the photons are massless and do therefore not couple to the Higgs-boson - and a fermion (or W-boson) loop is needed to mediate the process, reducing the branching ratio. The $b\bar{b}$ final state has a higher branching ratio than the WW^* despite the W-boson being heavier, because of kinematic suppression: One of the W-bosons must be off-shell, as $m_h < 2m_W$. For this analysis, the decays $h \to WW^*$ and $h \to \gamma\gamma$ are particularly relevant.

Table 2.2.: Calculated branching ratios of a Higgs-boson with $m_h = 125.09$ GeV [16].

Decay products	Branching Ratio	Uncertainty
$\gamma\gamma$	$2.270 \cdot 10^{-3}$	$\pm 1.73\%$
WW^*	$2.152 \cdot 10^{-1}$	$\pm 0.99\%$
ZZ^*	$2.641 \cdot 10^{-2}$	$\pm 0.99\%$
$b\bar{b}$	$5.809 \cdot 10^{-1}$	$\pm 0.65\%$
$\tau\tau$	$6.256 \cdot 10^{-2}$	$\pm 1.16\%$

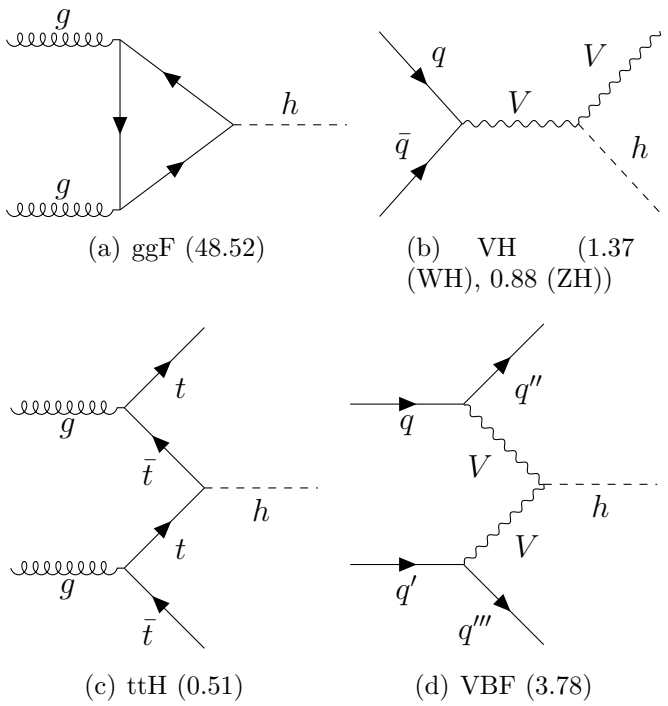

(a) ggF (48.52) (b) VH (1.37 (WH), 0.88 (ZH))

(c) ttH (0.51) (d) VBF (3.78)

Figure 2.4.: Leading-order single Higgs-boson production processes and their production cross sections in pb (for proton-proton colliders with $\sqrt{s} = 13$ TeV): (a) gluon gluon fusion, (b) associated production with a vector boson, V, (c) associated Higgs-boson production with top pair, (d) vector boson fusion. Various uncertainties on the cross section are listed in reference [16].

2.1.3. Limitations of the Standard Model

Despite its numerous successes, the Standard Model has a few limitations. It only incorporates three of the four known forces, as gravity cannot be quantized in a consistent way [17]. Neutrinos are considered to be massless in the SM, which is contradicted by observable neutrino oscillations [18]. The SM also cannot completely explain the baryon asymmetry which is apparent in the universe [19]. Furthermore the SM does not provide a candidate for dark matter. Next to these shortcomings of the SM, aesthetic problems also exist: For example, the SM does not provide an explanation for the huge discrepancy between the Higgs-bosons mass and the Planck mass (hierarchy problem), which requires fine tuning [20]: the mass renormalization of fundamental scalars is quadratically divergent. In order for the Higgs-boson to have a mass of around 125 GeV, this divergence must almost exactly cancel in perturbation theory.

Several ideas have been proposed to solve some of those problems. One of which is the introduction of a symmetry between bosons and fermions, adding for each fermionic (bosonic) particle a bosonic (fermionic) superparticle. This supersymmetry (SUSY) could

explain the hierarchy problem, as loop corrections to the Higgs-boson mass would naturally cancel [21]. If, in addition, one assumes that no supersymmetric particle (sparticle) can decay into only SM particles (R-parity conservation) the lightest sparticle is stable and therefore a candidate for dark matter.[22]

2.2. Two-Higgs-Doublet-Models

In the minimalistic supersymmetric extension of the Standard Model (MSSM), more than one Higgs doublet and therefore more than one Higgs-boson is required [11]. This is due to the fact that gauge anomalies would not cancel if only one Higgs-fermion (superpartner of the Higgs-boson) were added. A single doublet could also only generate the masses for up-type or down-type quarks but not for both. There are also non-supersymmetric Two-Higgs-Doublet-Models (2HDM) like the Peccei-Quinn Model [23].

Two complex doublets possess eight degrees of freedom, of which three are required to provide the masses for $W^{\pm}$ and Z^0. The remaining five degrees would lead to five Higgs-bosons: one neutral pseudoscalar, CP-odd boson, A, two neutral scalar CP-even bosons, h and H, and two charged scalar CP-even bosons, $H^{\pm}$ [11]. In the following H will be referred to as 'heavy Higgs-boson'.

One can denote the two complex Higgs doublets of 2HDM as [11]

$$\Phi_a = \begin{pmatrix} \Phi_a^+ \\ (v_a + \rho_a + i\eta_a)/\sqrt{2} \end{pmatrix},$$

for the two doublets $a \in \{1, 2\}$, v and η are identical to the discussion of one Higgs doublet but specific to the value of a. ρ is defined as (in the general form for n scalar multiplets):

$$\rho = \frac{\sum_{i=1}^{n}[(I_i(I_i+1) - \frac{1}{4}Y_i^2]v_i}{\sum_{i=1}^{n}\frac{1}{2}Y_i^2 v_i},$$

with the weak isospin I and the hypercharge Y.

Assuming CP-conservation, absence of spontaneous CP breaking and elimination of quartic terms by discrete symmetries, the most general scalar potential for the two doublets is:

$$
\begin{aligned}
V = m_{11}^2 \Phi_1^\dagger \Phi_1 + m_{22}^2 \Phi_2^\dagger \Phi_2 - m_{12}^2 (\Phi_1^\dagger \Phi_2 + \Phi_2^\dagger \Phi_1) \\
+ \frac{\lambda_1}{2} (\Phi_1^\dagger \Phi_1)^2 + \frac{\lambda_2}{2} (\Phi_2^\dagger \Phi_2)^2 + \lambda_3 \Phi_1^\dagger \Phi_1 \Phi_2^\dagger \Phi_2 \\
+ \lambda_4 \Phi_1^\dagger \Phi_2 \Phi_2^\dagger \Phi_1 + \frac{\lambda_5}{2} (\Phi_1^\dagger \Phi_2)^2 + \frac{\lambda_5}{2} (\Phi_2^\dagger \Phi_1)^2 .
\end{aligned}
$$

It can be shown, that the resulting mass terms for the scalars are given by:

$$
\mathcal{L}_{\rho,mass} = -P \begin{pmatrix} m_{12}^2 \frac{v_1}{v_2} + \lambda_1 v_1^2 & -m_{12}^2 + \lambda_{345} v_1 v_2 \\ -m_{12}^2 + \lambda_{345} v_1 v_2 & m_{12}^2 \frac{v_1}{v_2} + \lambda_2 v_2^2 \end{pmatrix} P^T ,
$$

with $P = (\rho_1, \rho_2)$ and $\lambda_{345} = \lambda_3 + \lambda_4 + \lambda_5$.

The mass squared matrix of the scalars is diagonalizable, the angle that performs this diagonalization is called α. Furthermore, one relevant parameter of 2HDMs is the quantity

$$
\tan \beta = \frac{v_1}{v_2} .
$$

2HDMs are usually grouped into types I and II, whereby type I 2HDMs assume that charged fermions couple only to the second doublet, while type II 2HDMs assume, that up- and down-type quarks couple to separate doublets. There are, however, also additional types, like type III, which allows for flavor changing neutral currents at tree level. The MSSM and the Peccei-Quinn Model both are of type II, this thesis will also implicitly assume a type II 2HDM.

2.3. Di-Higgs production

The Higgs self-interaction remains an important undetermined element of the spontaneous symmetry breaking [24]. Calculating the Higgs potential after the Higgs doublet is expanded around the vacuum expectation value yields trilinear and quartic h-vertices ($V \supset \frac{1}{2} m_h^2 h^2 + \sqrt{\frac{\eta}{2}} m_h h^3 + \frac{\eta}{4} h^4$). Those are proportional to $\sqrt{\eta}$ and η respectively, and therefore important to search for in order to determine the Higgs potential. The primary motivation for analyzing non-resonant Higgs pair production, is to measure the self coupling of the Higgs-boson. Feynman diagrams for non-resonant di-Higgs productions are shown in figure 2.5. At the LHC, the non-resonant production at $\sqrt{s} = 13$ TeV is expected

to have a cross section of approximately only 37.3 fb (at NNLO) [25], while several BSM theories, like strong electroweak symmetry breaking scenarios [26], predict an enhanced cross section. This motivates further study of di-Higgs productions, despite the fact that as of now not enough data has been collected to be sensitive to the SM cross section. The running of the production cross section for multiples of the SM Higgs-boson self-coupling parameter is shown in figure 2.6.

Furthermore, a heavy Higgs-boson, as described in section 2.2, could decay into a pair of SM Higgs-bosons $H \rightarrow hh$ and would therefore appear as a resonance. The Feynman diagram in figure 2.7 shows a process leading to such a resonant Higgs-Boson pair production [24].

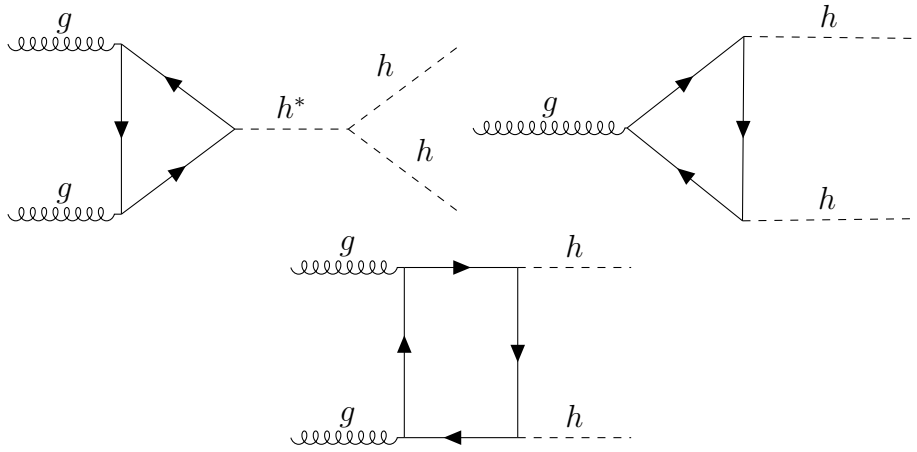

Figure 2.5.: Leading-order graphs for non-resonant di-Higgs production, a trilinear coupling in the gluon-gluon fusion is seen in the top left. Processes like the one on the top right yield only vanishing contributions, due to color conservation. The box diagram at the bottom interferes destructively with the trilinear gluon-gluon fusion. [27]

Investigations to set upper limits on the di-Higgs production for $\sqrt{s} = 13$ TeV are ongoing. Figure 2.8 shows the upper limits for $\sigma(hh \rightarrow b\bar{b}b\bar{b})$ for various values of m_H. Note however, that those results only use 3.2 fb^{-1} of data. Figure 2.9 shows the upper limit for low mass points in the decay channel $hh \rightarrow \gamma\gamma WW^*(l\nu jj)$, while figure 2.10 shows the upper limits for various channels for a center-of-mass energy of 8 TeV.

Upper limits for $\sqrt{s} = 13$ TeV are still being investigated - especially boosted final states are not yet analyzed in great detail. The goal is to combine various channels in order to achieve optimal upper limits for $\sqrt{s} = 13$ TeV for a variety of mass points, similar to the combination for $\sqrt{s} = 13$ TeV depicted in figure 2.10.

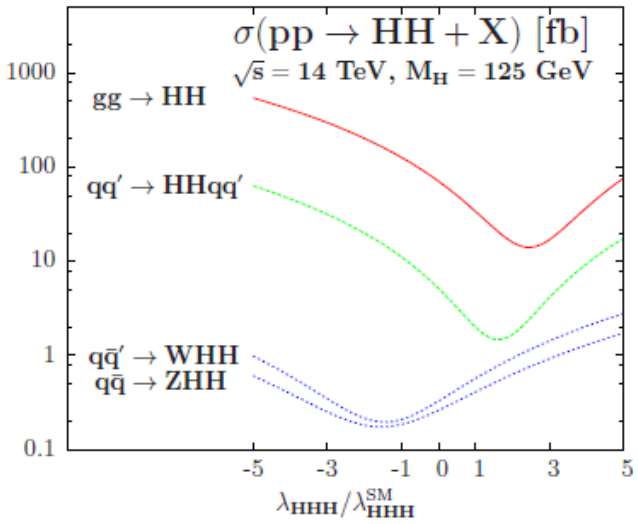

Figure 2.6.: Di-Higgs production cross section as a function of the Higgs-bosons trilinear coupling [24].

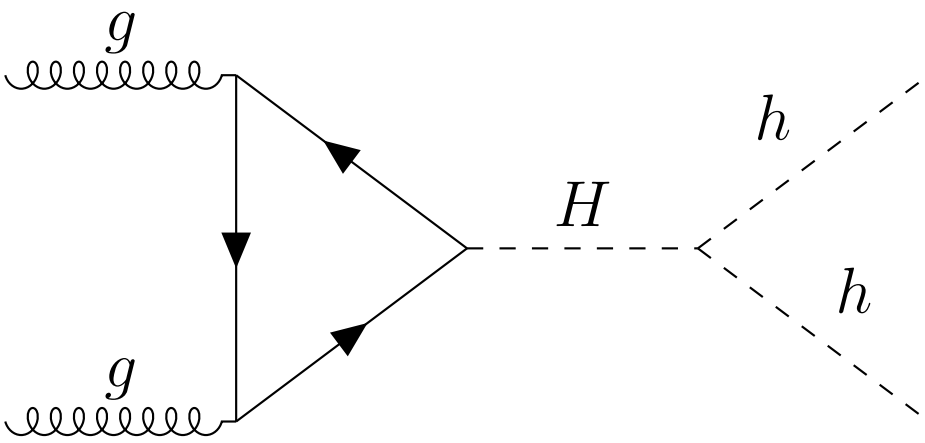

Figure 2.7.: Leading-order Feynman diagram for resonant Higgs-boson pair production.

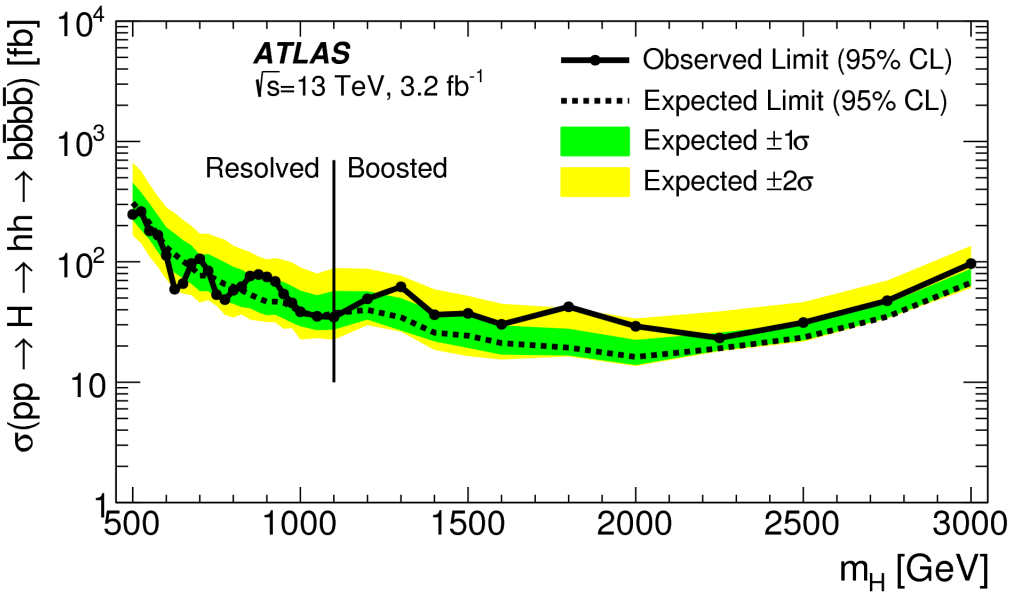

Figure 2.8.: Limits on the resonant di-Higgs production cross section times branching ratio for the 4b final state for $\sqrt{s} = 13$ TeV [28].

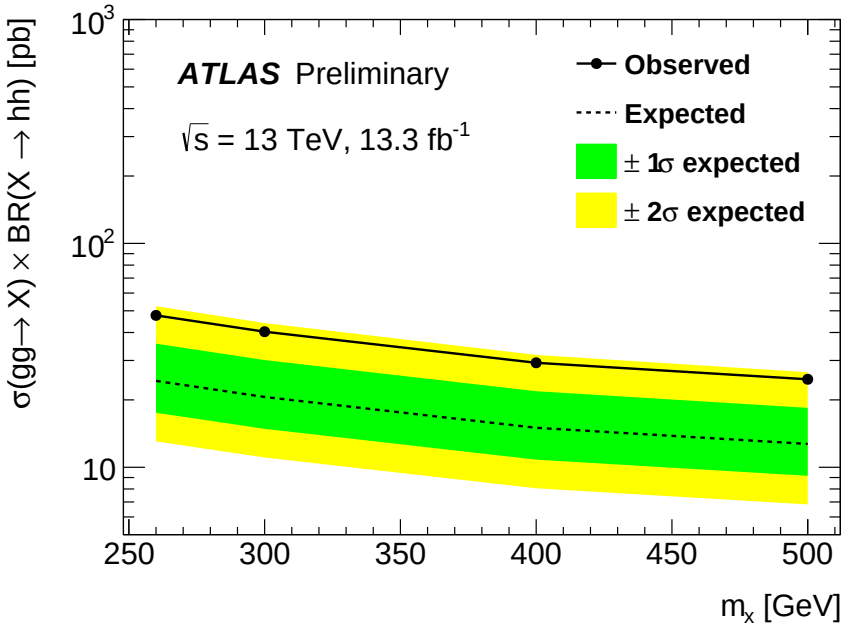

Figure 2.9.: Limits on the resonant di-Higgs production cross section for $\sqrt{s} = 13$ TeV, as measured in the channel $h \to \gamma\gamma WW^*$ [29].

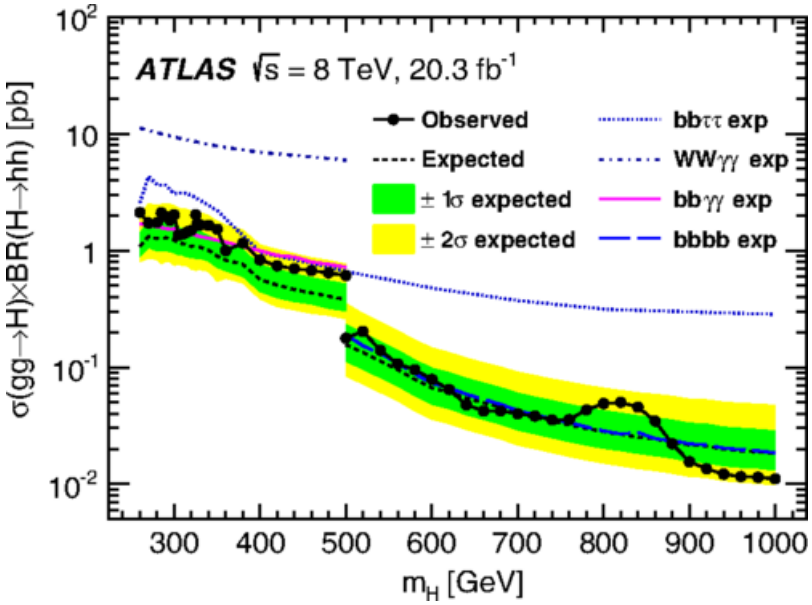

Figure 2.10.: Combined limits on the resonant di-Higgs production cross section for $\sqrt{s} = 8$ TeV [30].

3. Experimental apparatus and methods

3.1. LHC

The Large Hadron Collider (LHC) is an underground proton-proton (and heavy ion) synchrotron collider located at CERN near Geneva, Switzerland [31]. It currently operates at a center-of-mass energy of $\sqrt{s} = 13$ TeV with an instantaneous luminosity of the order of 10^{34} cm^{-2}s^{-1}. It accelerates protons to nearly the speed of light, c, and has a circumference of 27 kilometres. Two beams of protons travel in opposite directions through the accelerator ring. Collisions occur at four different interaction points where the two beams cross. In experiments positioned at those collision points, the collision events are studied, usually by detecting the final decay products of unstable particles created in proton-proton interactions. These experiments are ATLAS [32], CMS [33], LHCb [34] and ALICE [35].

The LHC uses a series of acceleration steps to accelerate protons to the desired 6.5 TeV beam energy. The acceleration chain is depicted in figure 3.1: Ionized hydrogen atoms (protons) are accelerated to 50 MeV by the LINAC2 and from there to 1.4 GeV by the Proton Synchrotron Booster. In the Proton Synchrotron they are then accelerated to 25 GeV and lastly by the Super Proton Synchrotron to 450 GeV. With this energy they can be injected into the LHC ring, with a bunch spacing of 25 ns. There are nominally 2808 total bunches along the ring with 10^{11} protons each. The LHC provides the final acceleration to 6.5 TeV.

3.2. ATLAS

The ATLAS (A Toroidal LHC ApparatuS) experiment is the largest experiment at the LHC [31, 32]. A diagram of the detector is shown in figure 3.2. The detector is built symmetrically around an interaction point and has roughly cylindrical shape. A right handed coordinate system is overlaid using the direction to the center of the collider as

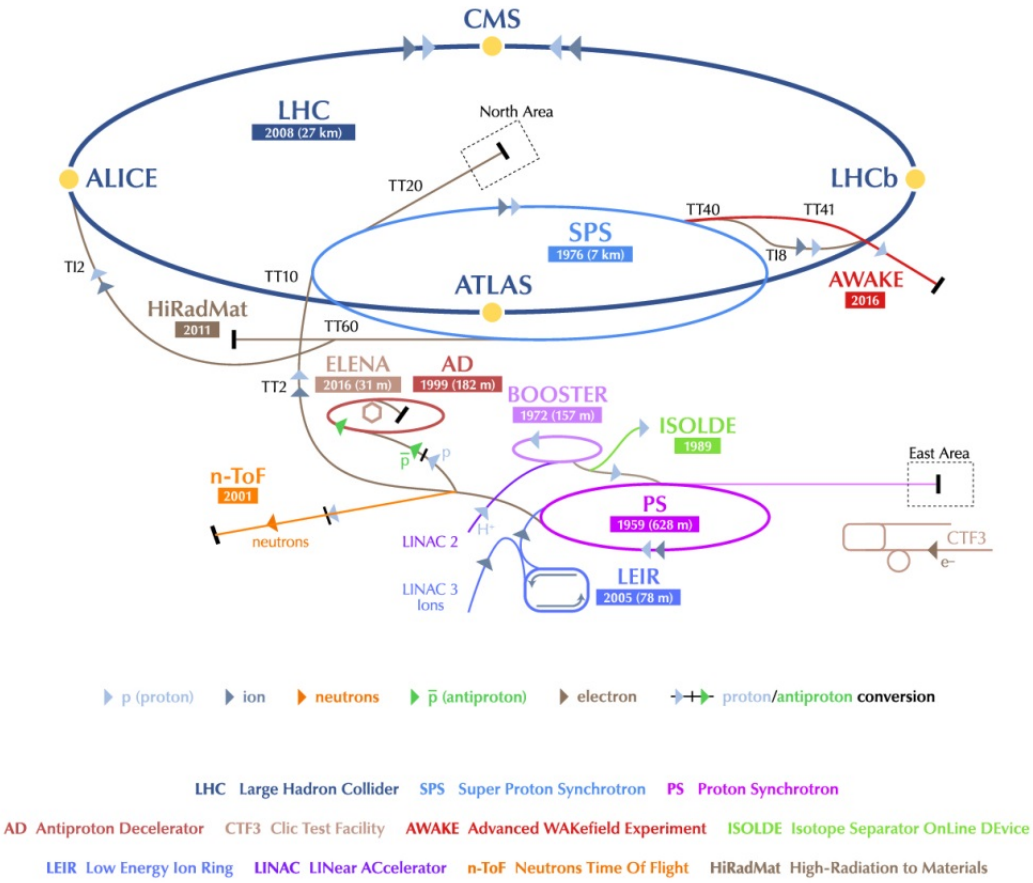

Figure 3.1.: Scheme of the LHC, showing the acceleration chain as well as the location of several experiments [36].

positive x direction and the upward direction as positive y direction, such that z points along the beam line. A particle's momentum perpendicular to the z-axis is denoted as p_T. One usually defines a cylindrical coordinate system with the origin at $z = 0$. The azimuthal angle, ϕ, is then the angle in the x-y-plane, whereby $\phi = 0$ coincides with the y-axis. The polar angle, θ, is the angular distance from the $+z$-axis. As the particles are accelerated to speeds close to the speed of light, it is reasonable to use the pseudorapidity $\eta = -\ln(\tan\frac{\theta}{2})$ instead of θ, as differences in pseudorapidity are Lorentz invariant for boosts along the direction of the beam.

The ATLAS detector [32] has a mass of about 7000 tons and is located in a cavity approximately 100 meters below ground at CERN. The detector is built, such that it provides a high level of hermicity, allows for high precision energy and momentum measurements and is able to provide identification of different particle types based on their signature. It consists of several layers and many different detector systems, some of which will be described in the following. The resolutions and coverage of each detector system

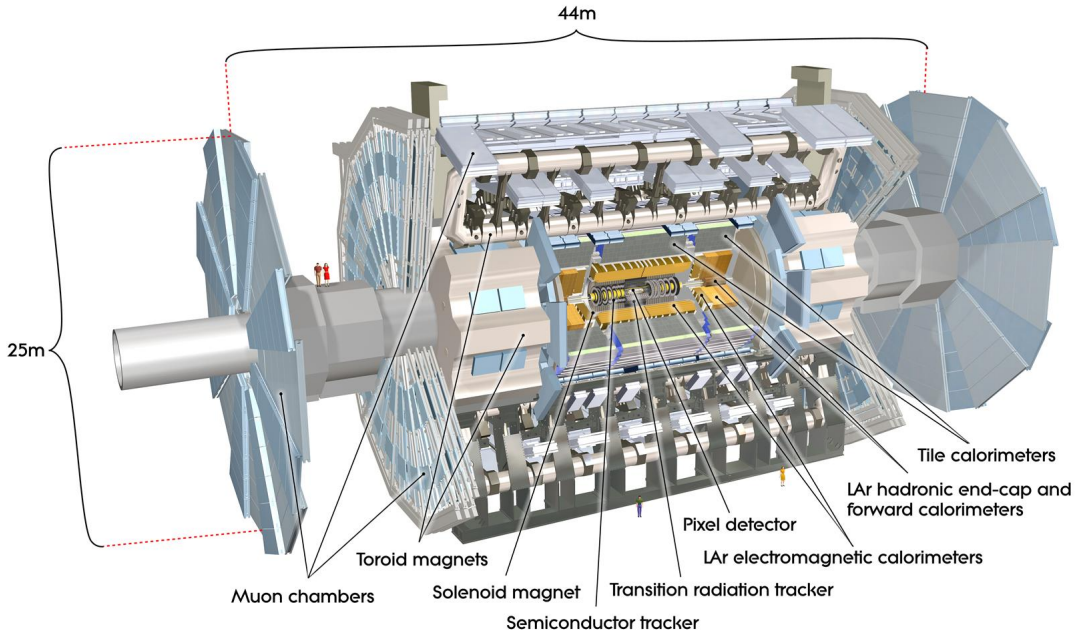

Figure 3.2.: Diagram of the ATLAS detector, showing the different layers and detector systems [37].

is listed in table 3.1. The inner detector is the layer closest to the interaction point and consists of the silicon pixel detector, the Semiconductor Tracker and the Transition Radiation Tracker. The inner detector is used to measure the momentum and charge of each charged particle and is therefore covered by a magnetic field of 2 T, created by a central solenoid. The deflection of a charged particle due to this magnetic field is dependent upon charge and momentum of the particle.

The electromagnetic and hadronic calorimeters are located around the inner detector. The electromagnetic calorimeter is a sampling calorimeter using liquid Argon and lead. Mostly electrons and photons deposit their energy in this calorimeter due to bremsstrahlung and electron pair production and subsequent shower production. The hadronic calorimeter consists of tile- forward and end-cap calorimeters, using iron and plastic scintillator, tungsten and liquid argon and iron and liquid argon respectively. In the hadronic calorimeter, particles lose energy by elastic and inelastic nuclear scattering and produce a spray of secondary particles, which again undergo scattering processes and produce further particles. Decaying particles can also produce electromagnetic showers inside the hadronic shower. Ideally, all the particles (except for muons and neutrinos) deposit their energy in the calorimeters, such that by combining all energy deposits into clusters, one is able to obtain a proxy for the particles energy.

The outermost layer of the detector is a system of muon chambers. Muons as minimal ionizing particles lose only a small fraction of their energy in the calorimeter and can therefore be detected in proportional chambers in the muon layer. Tracks in those chambers can then be used to identify muon tracks in the tracker or muon energy deposits in the calorimeter. The outermost parts of the detector are also covered by a magnetic field, which is created by toroidal magnets. Those provide fields with 3.9 T (end-cap toroid) and 4.1 T (barrel toroid).

The acquired data is filtered before further processing, as the collision rate of 40 MHz is too high to record and store every single event. The filtering is done in several triggering steps. The trigger system checks for example for the presence of high-p_T particles in form of clusters, leptons or missing transverse energy, or for several combinations of particles with certain energy and p_T thresholds. As a last step, a so called high-level trigger is used, reconstructing the event in-time and only accepting specific signatures. Finally about 1000 events are recorded per second. Those events are later used for analysis.

Table 3.1.: Resolution and coverage of the different parts of the ATLAS detector [32], with E being the energy of the corresponding object, σ its uncertainty and p_T its transverse momentum. The momentum resolution of the muon system is highly inhomogeneous, the stated value is an upper limit for about 80% in the phase space between 10 GeV $\leq p_T \leq$ 300 GeV.

Detector part	Resolution	Coverage in η
Inner detector	$\sigma_{p_T}/p_T = 0.05\ \% p_T \oplus\ 1\%$	$\lvert\eta\rvert \leq 2.5$
EM calorimeter	$\sigma_E/E = 10\%/\sqrt{E} \oplus\ 0.7\%$	$\lvert\eta\rvert \leq 3.2$
Had calorimeter (tile, end-cap)	$\sigma_E/E = 50\%/\sqrt{E} \oplus\ 3\%$	$\lvert\eta\rvert \leq 3.2$
Had calorimeter (forward)	$\sigma_E/E = 1/\sqrt{E} \oplus\ 0.7\%$	$3.1 \leq \lvert\eta\rvert \leq 4.9$
Muon spectrometer	$\sigma_{p_T}/p_T = 0.05$	$\lvert\eta\rvert \leq 2.7$

3.3. Simulation methods

Monte Carlo [38] generators are used to model physical events by simulating the matrix element (of the simulated primary interaction), the parton showering and the underlying event (interactions in the same bunch crossing, other than the simulated primary event). The results from this simulation are stored in the so-called truth record, a description of the true particles before detector effects come into play. With a simulation of the ATLAS detector, those results are mapped to a simulated detector response of the event in question. This is stored in the same way as the actual data and therefore allows for direct comparison between data and simulation.

The simulation of the ATLAS detector is performed using GEANT4 [39]. However, different approaches are possible: On the one hand, a full simulation can be performed, which models every aspect of the detector to a very high level of accuracy. On the other hand, an fast simulation (AFII) [40] can be performed, which focuses on the most important elements and less precise but computationally faster approximation methods. The simulation of the tracking detector is identical in fast and full simulation, while the calorimeter simulation is not. Instead of modelling particle interactions with matter in the calorimeter, a parametrized description of the calorimeter is used to estimate the detector's response. In AFII, the total momentum of a hadron spray is well-modeled, as the amount of incoming energy is set by generator and parton showering. However, the number of clusters as well as the energy distribution across clusters differs substantially from the full simulation.

3.3.1. Signal simulation

For the signal, MC samples for non-resonant as well as for resonant di-Higgs production with $hh \to \gamma\gamma WW^*$ for several heavy Higgs mass points (260 GeV $\leq m_H \leq$ 3 TeV) were used. They all rely on fast simulation. The generators for the signal samples are `Madgraph5_aMC@NLO` [41] (matrix element) and Herwig ++ [42] (hadronization, showering, underlying event), with the `CTEQ6L1` PDF set [43]. The PDF tune is `UEEE5` [41].

Table 3.2 shows the number of events in a selection of the signal samples, as well as cross section times branching ratio $\sigma \cdot BR(hh \to \gamma\gamma WW^*)$ for an assumption of $\sigma = 1$ pb. A complete list of the samples' names, also including validation samples is given in appendix A.5.

Table 3.2.: Summary of the signal samples for non-resonant production and resonant productions for several values of m_H, assuming standard model like behavior of the di-higgs system [1]

Mass point m_H[GeV]	Number of generated events	$\sigma \cdot BR(hh \to \gamma\gamma WW^*)$ [fb]
non-resonant	970000	0.98
500	179000	0.98
750	184000	0.98
1000	200000	0.98
1500	195000	0.98
2000	179000	0.98
2500	197000	0.98
3000	199000	0.98

3.3.2. Background simulation

For this analysis, SM background $h \to \gamma\gamma$ MC samples were used. For the background the Higgs-boson production modes ggF (gluon-gluon-Fusion), VBF (vector boson fusion), $t\bar{t}H$ (associated top pair production), ZH and WH (Higgsstrahlung) were used.

The matrix elements for the ggF and VBF background samples are calculated using Powheg [44] and Pythia8 [45] is used for showering, hadronization and underlying event calculations. The `CT10` [46] PDF set with tune `AZNLOCTEQ6L1` [47] is used. For VH and $t\bar{t}H$, the Pythia8 generator and PDF `NNPDF23LO` [48] with `A14NNPDF23LO` [49] tune were used.

Table 3.3 shows the number of events in the background samples as well as production cross section times branching ratio $\sigma \cdot BR(h \to \gamma\gamma)$. A complete list of the samples' names is given in appendix A.5.

Table 3.3.: Background SM $h \to \gamma\gamma$ samples, assuming again standard-model-like behavior of the di-higgs system [1].

Channel	Number of events	$\sigma \cdot BR(h \to \gamma\gamma)$ [fb]
ggF	1930000	110.1
VBF	984000	8.6
WH	246200	3.1
ZH	247800	2.0
ttH	49800	1.2

3.4. Hadronic jet reconstruction

Unbound partons produce showers of a multitude of hadrons, which in turn deposit energy in the calorimeter. The reconstruction of the original parton follows an inversion of the physical process: Depositions are combined into clusters with the goal that each cluster contains the energy depositions of one hadron. The clusters are then combined in order to obtain information about the original parton. This combination of clusters is an object called jet and there are several methods to construct a jet with different sets of advantages and disadvantages. One class [50] of sequential clustering algorithms is described in the next section (3.4.1).

3.4.1. Jet reconstruction

The inputs for the k_t reconstruction algorithm [50] (and its variations) are charged particle tracks, energy clusters or truth hadrons - in this analysis clusters only relying on

information of the calorimeters are used (called LCTopo clusters). In the following the input objects are referred to as protojets. The algorithm lists for every protojet the quantity d_{iB} and for every possible permutation of two protojets, i and j, the quantity d_{ij} as follows:

$$d_{ij} = \min(p_{T,i}^{2p}, p_{T,j}^{2p}) \frac{\Delta R_{ij}^2}{R^2}$$
$$d_{iB} = p_{T,i}^{2p}$$

Where $p_{T,i}$ is the transverse momentum of protojet i, $\Delta R_{ij}^2 = (y_i - y_j)^2 + (\phi_i - \phi_j)^2$ is a measure of the angular separation between the two protojets, with the rapidity y, defined as: $y = \frac{1}{2} \ln\left(\frac{E+p_z}{E-p_z}\right)$, whereby E and p_z are the protojet's energy and momentum along the z-axis. R is a measure for the size of the jet cone. The parameter p defines different algorithms, while $p = -1$ corresponds to the anti-k_t algorithm which was used to construct the jets for this analysis, $p = +1$ corresponds to the k_t algorithm, which is used in the construction of the substructure variables called N-subjettiness, see section 3.4.4. The parameter p is a measure for the relative power of energy versus geometrical scale.

If now the smallest calculated value in the list is of the type d_{ij}, the protojets i and j are combined (they produce a new protojet which has the added four-momenta of i and j). If it is of type d_{iB}, i is called a jet and removed from the list of protojets. After this step the list is updated as the set of protojets changed. This procedure is repeated until no protojets are left.

There is no perfect algorithm. How they combine the same clusters in the y-ϕ plane is depicted in figure 3.3. The k_t algorithm approximates the inversion of QCD branching processes, by first combining the smallest energy depositions, while the anti-k_t algorithm yields cone-shaped jets, which as they start reconstruction from high energies are less sensitive to pile-up and the underlying event.

3.4.2. Jet mass, calibration, grooming

For a jet based on calorimeter-cell clusters, J, with cluster constituents, $\{i\}$, the calorimeter-based jet mass, m^{calo}, is defined as:

$$m^{\text{calo}} = \sqrt{\left(\sum_{i \in J} E_i\right)^2 - \left(\sum_{i \in J} \vec{p}_i\right)^2}$$

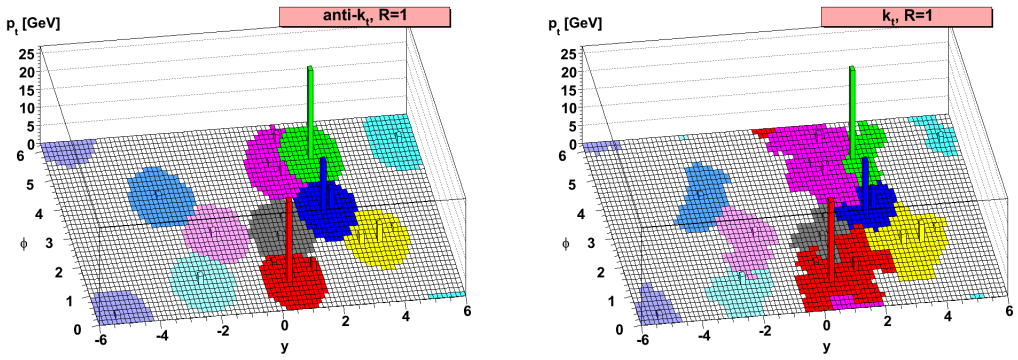

Figure 3.3.: Jet reconstruction using the anti-k_t and k_t algorithms. The methods are similarly valid but differ substantially in their results. Energy depositions are shown in the $y - \phi$ plane with their p_T depicted on the z-axis. The different colors represent different jets. The exact same MC generated event was used [50].

with E_i and $\vec{p}_i$ being the energy and momentum of cluster i.

To in addition utilize tracking information, the so called track-assisted jet mass, m^{TA}, is used. For the definition, an association between jets and tracks is necessary, which is done using so called ghost-matching. Ghost-matching is a procedure, which does not directly rely on a matching from jet to a given track with a ΔR criterion. Instead the track in question is added with an infinitesimal energy to the input of the jet algorithm. If the algorithm includes the track in the jet, the jet and track are ghost-matched.

The track-assisted jet mass, m^{TA} is defined as:

$$m^{\mathrm{TA}} = \frac{p_T^{\mathrm{calo}}}{p_T^{\mathrm{track}}} \cdot m^{\mathrm{track}}.$$

Here p_T^{calo} is the transverse momentum of the calorimeter jet. For the associated tracks, the four-vector sum is calculated: p_T^{track} is the transverse momentum and m^{track} is the invariant mass of this sum.

Electromagnetic showers will also be produced inside hadronic showers. This effect as well as the necessity to use sampling calorimeters (to reduce cost and to separate the function of producing a particle signal (deposition) and reading it out) and a finite detector length make a recalibration necessary (EM-scale calibration). Additionally nuclear reactions, i.e. the creation of new bound states, occur which result in the fact, that hadronic interactions inherently involve undetectable energy deposits. This requires additional calibration, which is done on the energy cluster level.

When the jets are constructed, they also have to be calibrated in order to compensate for further effects related to the detector design. To calibrate the energy of a jet, a comparison is performed between the reconstructed jet energy to the energy of a corresponding truth level jet (in MC) and the reconstructed jet energy is scaled accordingly. This calibration is executed by studying γ+jet events, in which the photon can be well measured. Due to momentum balance this yields information about the recoiled jet. A jet mass scale calibration is performed against known mass peaks like W-boson and t-quark [51–54].

For large radius jets (see sec. 3.4.3) a correction also has to be applied to account for the underlying event or pile-up (additional processes, which do not stem from the primary interaction in question). For this, a grooming procedure is applied [55]. As with the jet reconstruction algorithms, there is no single correct way to reduce pile-up from a jet and consequently several methods are available. The algorithm used in this analysis is called trimming [56] and is depicted in figure 3.4. Using the k_t algorithm with a distance parameter R_{sub}, the constituents of the jet in question are combined into subjets. Subjets with a p_T below a certain percentage of the total jet's p_T, f_{cut}, are discarded: All associated clusters are ignored when the total jet is reconstructed. In this analysis the following values are used for large radius jets: $f_{\text{cut}} = 0.05$ and $R_{\text{sub}} = 0.2$.

For small radius jets (anti-$k_t(R = 0.4)$), no grooming is applied, but rather a JetVertexTagger (JVT) [57] is used to determine if they stem from pile-up effects.

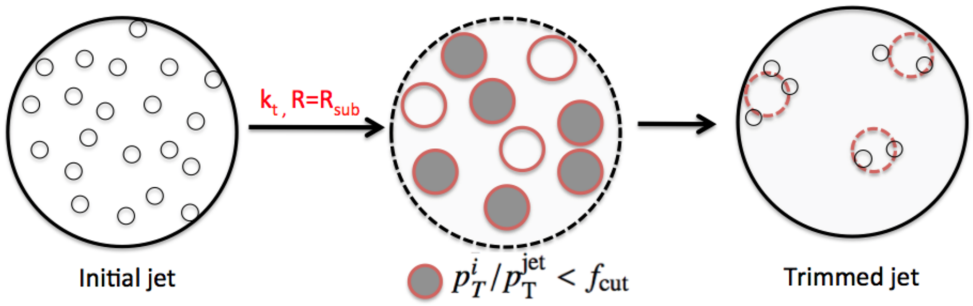

Figure 3.4.: Depiction of the grooming method called trimming [56]. From the constituents of an initial jet, the k_t algorithm with $R = R_{\text{sub}}$ is used to build subjets. Subjets with a p_T below a percentage of the total jet p_T, f_{cut} are discarded. The trimmed jet is reconstructed from the constituents of all the remaining subjets.

3.4.3. Large radius jets

At ATLAS, the nominal size parameter for anti-k_t jets is $R = 0.4$. This aims to resolve individual jets which originate from original partons in the collision. For a two-body-decay, the higher the momentum of the mother particle, the closer the four-momenta of the daughter will be in the lab frame. A rough estimate for the angular separation ΔR between the two daughters is $\Delta R \approx 2m_M/p_{T,M}$ (for negligible masses of the decay products) with the mother particle's mass m_M and transverse momentum $p_{T,M}$. A W-boson with $p_T = 400$ GeV could therefore decay into two quarks with an angular separation of $\Delta R \approx 0.4$, equal to the size parameter of an anti-$k_t(R = 0.4)$ jet. This results in the fact, that highly boosted topologies of resonant di-Higgs production at the order of $m_H = 1$ TeV cannot be resolved using one anti-$k_t(R = 0.4)$ jet for each parton.

When using anti-$k_t(R = 1.0)$ jets, one aims to include several partons of a given decay inside one jet and can then introduce substructure variables (see sec. 3.4.4) to obtain additional information to help identify the origin of the jet. Those jets are referred to as 'large radius jets', meaning jets with a large size parameter R. Note however, that despite this naming convention, the size parameter is not identical with the jet's radius.

In this study fast simulation methods were also used to create Monte Carlo samples as described in sec 3.3. The modeling of tracks is identical in the fast and the full simulation, while the simulation of the calorimeter response differs. Therefore, track-assisted mass was used in this analysis. The different performances in fast and full simulation of calorimeter mass and track-assisted mass are shown in figure 3.5. Another reason to use track-assisted mass is, that tracks can be resolved, even when they are very close to one another - whereby when energy clusters are merged, information is lost.

3.4.4. Jet substructure

Substructure variables are based on information on the energy distribution inside a jet and can help to identify the nature or origin of the jet. There is a multitude of substructure variables, of which one is used in this analysis. The goal of the variable called N-subjettiness is to obtain information as to how many prongs are included in a given jet. This aims to investigate the number of initial partons, grouped together into one single jet. N-subjettiness is a p_T weighted sum of angular distances between the jet constituents and N subjet axis. Such subjets are calculated using the k_t-algorithm. The value τ_N is calculated by reclustering all constituents of the jet into exactly N subjets and calculating the average distance between each constituent and the closest subjet. N-subjettiness τ_N is defined as:

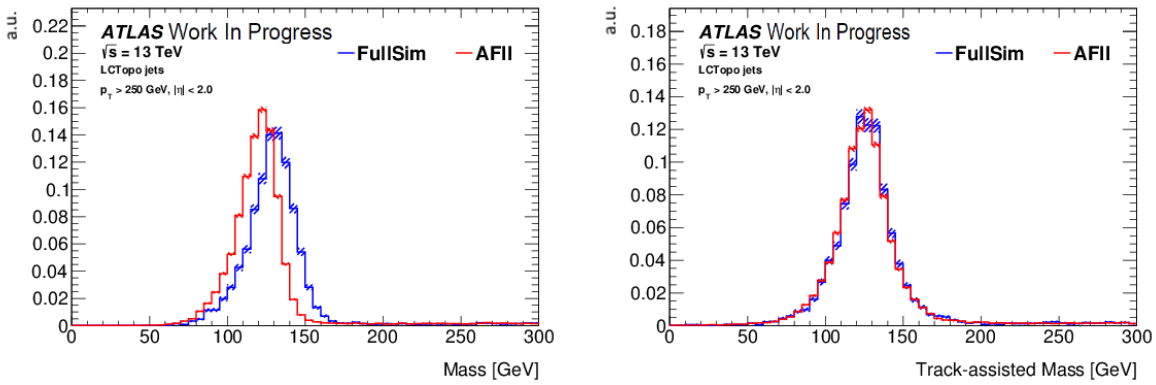

Figure 3.5.: Performance of the two mass definitions described in section 3.4.2 in the context of fast and full simulation. Depicted is the mass peak of the Higgs-boson, reconstructed by one large radius jet. The track-assisted mass is less sensitive to the type of simulation.

$$\tau_N = \frac{1}{d_0} \sum_{i \in J} p_{T,i} \min(\Delta R_{k,i} | k = 1, ..., N)$$
$$d_0 = \sum_{i \in J} p_{T,i} R_0$$

for subjets i and jet J.

When every subjet is close to all of the constituents it is composed of, τ_N remains small, as soon as a 'wrong' constituent is grouped to a subjet, the value increases sharply. So the calculation of τ_N gives a lower limit on the number of subjets: If a jet is best described containing N subjets, the variable τ_N should be much smaller than τ_{N-1}. The interesting value to study is therefore their ratio. If one expects a N-prong jet (with $N > 2$) but a significant number of events in which only $N-1$ prongs are reconstructed, one can utilize the product of τ_N/τ_{N-1} and τ_{N-1}/τ_{N-2}, or simply τ_N/τ_{N-2}.

To base the substructure variables on the track information, the ghost-matched tracks of a jet are used to construct a purely track-based version of the same jet. From this, the track based substructure variables can be calculated. This also aims to reduce sensitivity to the simulation type (fast or full simulation). Figure 3.6 shows a comparison of a purely track-assisted and a nominal substructure variable in dependence of simulation type. It can be concluded, that the sensitivity on simulation type is much smaller for the track-based substructure variable.

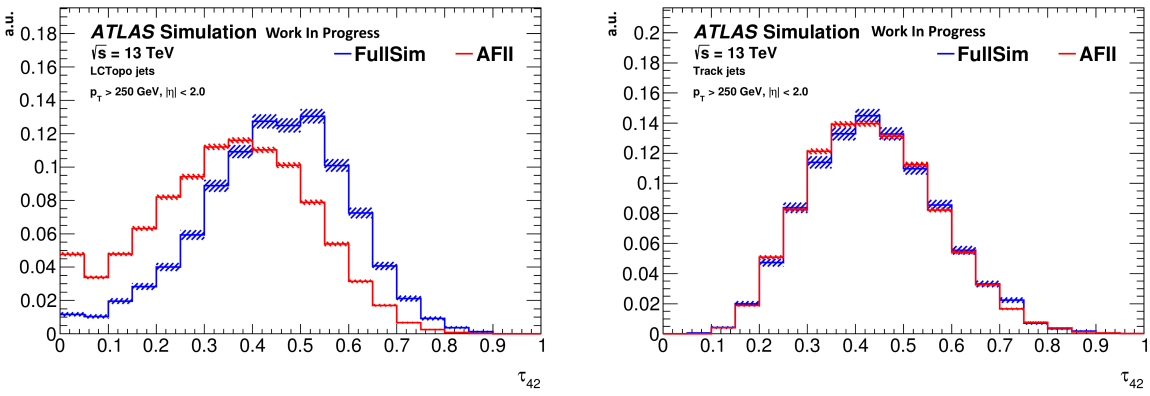

Figure 3.6.: Performance of nominal and purely track-based substructure variable τ_{42} for both simulation types. Track-based substructure is largely insensitive to using AFII, while the nominal substructure shows strong deviation from the full simulation results. Used are anti-$k_T(R = 1.0)$ jets.

4. The process $hh \to \gamma\gamma WW^*$ and selection criteria

4.1. Boosted event topology

This analysis focusses on the channel $hh \to \gamma\gamma WW^*$, with hadronically decaying W-bosons (see figure 4.1) with a boosted topology. The choice of the channel is motivated on the one hand by low background and high resolution of the decay $h \to \gamma\gamma$ and on the other hand on the high branching ratio of $h \to WW^*$, second only to $h \to b\bar{b}$ (see table 2.2). Since the processes $h \to WW^*$ and $h \to \gamma\gamma$ have already been observed and are consistent with SM prediction [9, 58], this analysis is suited to investigate BSM models like those predicting a heavy Higgs-boson, H, with a $H \to hh$ vertex. The decision to focus on hadronically decaying W-bosons is also motivated by the larger branching ratio, $BR(W \to qq') \approx 67\%$. The final branching ratio of $hh \to \gamma\gamma W_{had}W^*_{had}$ is 0.044 % [16].

Furthermore, due to the fact, that high resonance mass points have not yet been investigated in this channel, a boosted topology is studied, where the decaying SM Higgs-boson ($h \to WW^*$) is boosted such that its (final) decay products cannot be resolved using the Anti-$k_t(R = 0.4)$ jet as described in chapter 3.4.3. Heavier resonances, result in higher p_T of the Higgs-bosons, such that the decay products, which are produced back-to-back in the frame of the mother particle, are close to one another in the lab frame, due to the Lorentz boost of high p_T particles.

At this point three possible approaches were considered (see figure 4.2):

- Focus on the fully boosted topology, where all four partons are reconstructed in one large radius jet.
- Focus on the semi boosted topology, where each pair of partons stemming from one W-boson is reconstructed as one large radius jet.
- Select inclusively, such that both topologies are considered.

To allow for radiated jets (i.e. jets stemming from radiated gluons), it was decided to not focus on exactly one or exactly two large radius jets. The remaining options were to

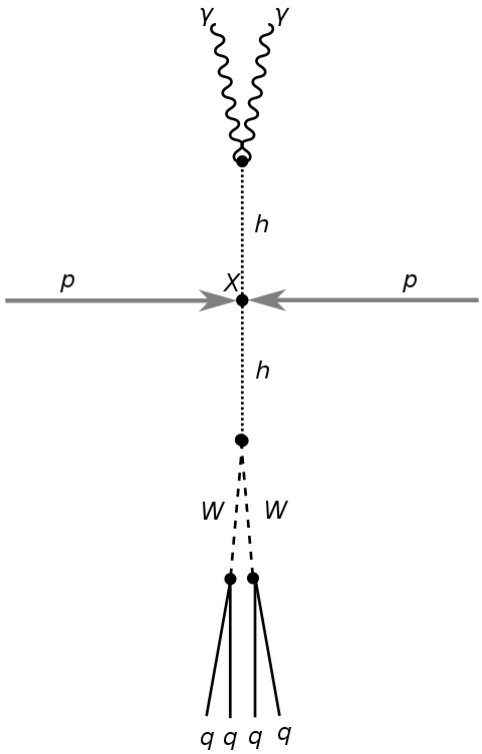

Figure 4.1.: Depiction of the resonant topology: In a proton proton collision a heavy scalar resonance X is produced and decays into two light Higgs, h, which in turn decay in WW and $\gamma\gamma$. The W-bosons decay hadronically. As the system is boosted, the final quarks are drawn close together.

select events with at least one large radius jet (i.e. allow for both topologies) or to select at least two large radius jets. The former was chosen for two reasons: On the one hand, the expected maximal distance between two partons, which are farthest away from each other can be estimated to be on the order of the size parameter of one large radius jet (for a heavy resonance at $m_H \approx 1$ TeV). On the other hand, the jet multiplicity in several signal samples was checked, also showing a significant number of events with only one large radius jet.

The distance between decay products, p_1 and p_2, from parent particle, M, can be estimated by $\Delta R(p_1, p_2) \approx \frac{2m_M}{p_{T,M}}$, if the masses of the decay products are negligible. Assuming an even splitting of p_T through the whole process (i.e. the p_T of both Higgs-bosons is identical and the p_T of both W-bosons is identical), the ΔR between the two W-bosons, W_i, for a heavy Higgs-boson with $m_H = 1$ TeV is expected to be roughly

$$\Delta R(W_1, W_2) \approx \frac{2 \cdot 125}{500} = 0.5,$$

while the partons from each W-boson, W_i, are separated by

$$\Delta R(p_{i,1}, p_{i,2}) \approx \frac{2 \cdot 80}{250} = 0.64.$$

For the maximal estimated distance of the farthest two partons (arbitrarily chosen to be $p_{1,1}$ and $p_{2,2}$), one can assume a completely planar decay (all decays are in the same plane). So for the farthest estimated distance for $m_H = 1$ TeV, one obtains:

$$\Delta R(p_{1,1}, p_{2,2}) \approx \Delta R(W_1, W_2) + \frac{1}{2} \cdot \Delta R(p_{1,1}, p_{1,2}) + \frac{1}{2} \cdot \Delta R(p_{2,1}, p_{2,2}) = 1.14$$

.

This maximal distance is close to the distance parameter of one Anti-$k_t(R = 1.0)$ jet, which makes a successful resolution into two large radius jets unlikely. However, it must be noted, that this estimation assumes the masses of the decay products to be negligible compared to the mother particle. This is only true for $H \to hh$ and the hadronic decay of the W-boson, but not for the vertex $h \to WW^*$. Consequently the presented estimation only yields a hint, as to what topology is dominant and requires further investigation of the jet multiplicity.

Figure 4.3 shows the jet multiplicity for signal samples. The ratio between the number of events with one large radius jet and those with two large radius jets, is roughly 2 for the investigated resonant di-Higgs processes, while roughly 4 for the non-resonant production. The fully boosted topology is therefore not negligible, but dominant. By requiring at least one large radius jet, this analysis is sensitive to both the fully boosted and partially boosted topologies.

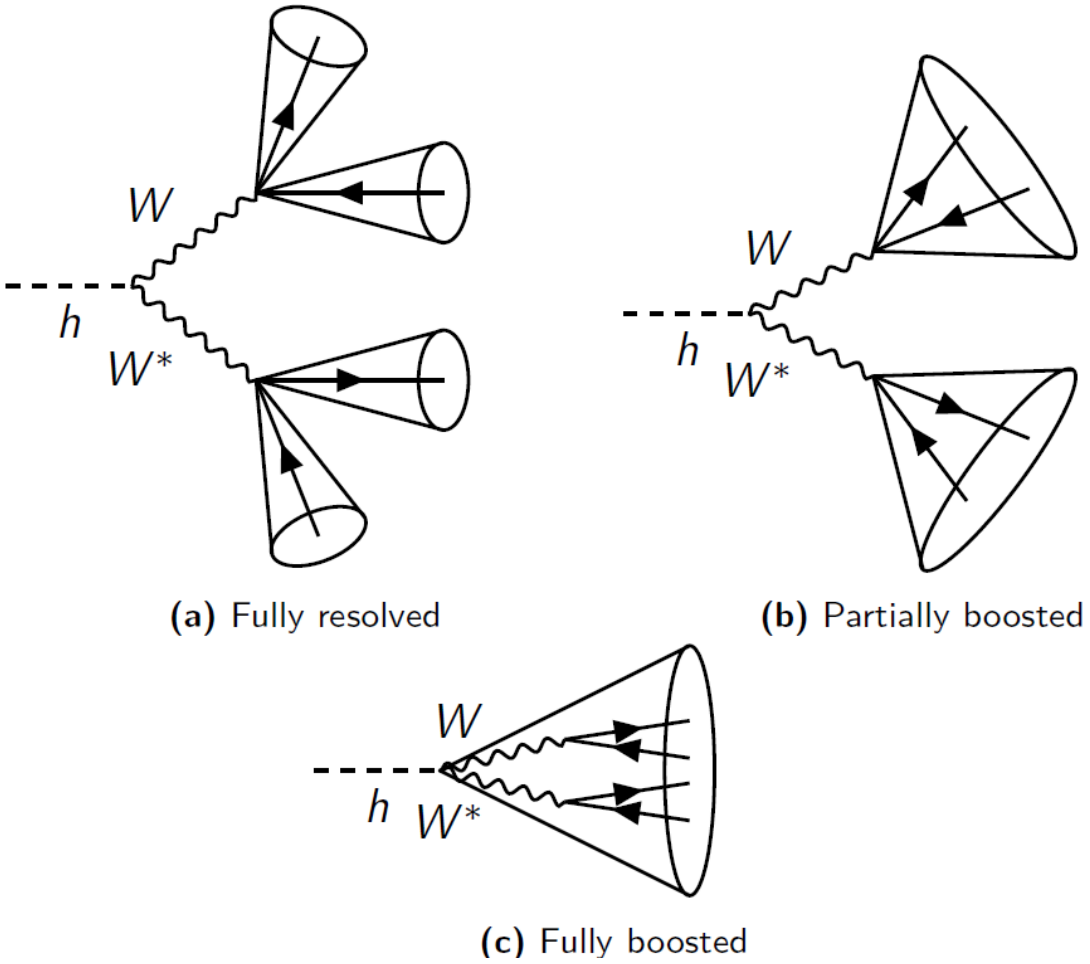

Figure 4.2.: Idealization of different topologies of $h \to W_{had}W^*_{had}$: (a) All partons are resolved with small radius jets, (b) the two parton pairs stemming from W-bosons are reconstructed with one large radius jet each and (c) all partons from the initial Higgs-boson are reconstructed in one large radius jet (c).

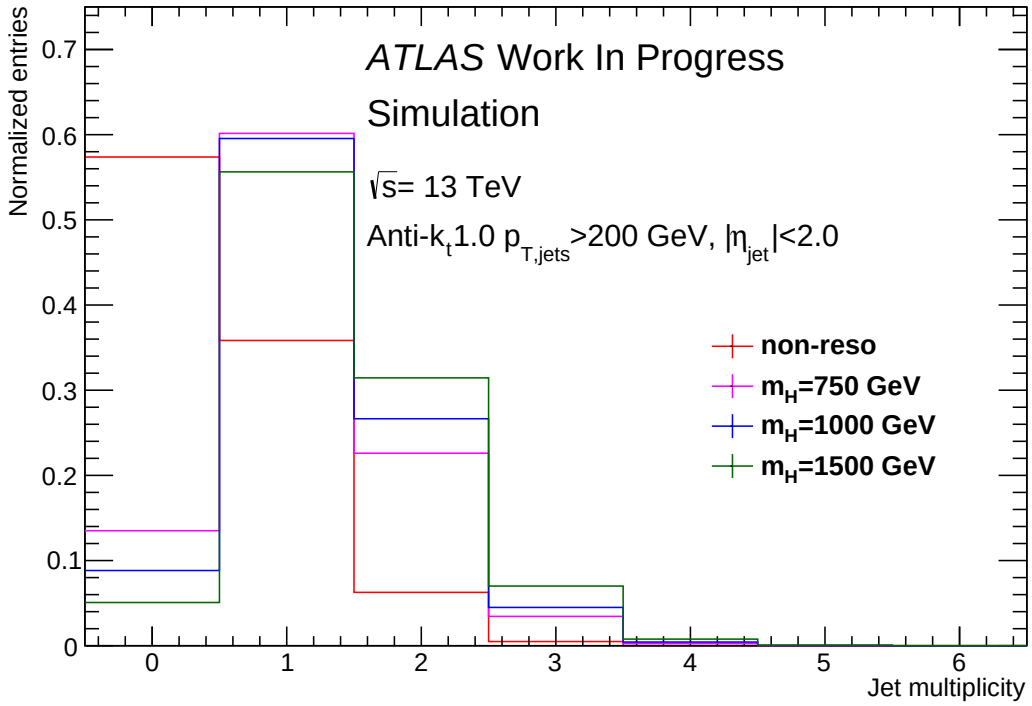

Figure 4.3.: Anti-k_t ($R = 1.0$) jet multiplicity in the signal sample for non-resonant di-Higgs production, as well as for three different resonant mass points. It can be concluded, that the fully boosted topology can not be neglected. Consequently an inclusive selection of both topologies is chosen.

4.2. Object definitions

From the signals of the various detector elements, objects are defined. These objects aim to represent the physical particles, that produced the signals in the detector.

4.2.1. Photons

Photons are reconstructed in two different ways: Either by reconstructing from energy clusters in the electromagnetic calorimeter, or by matching tracks in the inner detector with those energy clusters. The latter is only possible when the photon indirectly creates two tracks, which occurs when the photon is converted into an electron-positron-pair ($\gamma \to e^+e^-$) in the inner detector. For unconverted photons the reconstruction of energy clusters with no associated track is necessary. The particle identification working points 'Loose' and 'Tight' [59] are used. The latter is the final requirement on the photon ID and has an expected efficiency of ∼89%. Furthermore, the isolation criterion 'FixedCutLoose' [59] is used. In this analysis only photons are considered which possess the following properties: $|\eta| < 2.37$, $|\eta| \notin \{1.37, 1.52\}$, $p_T > 25$ GeV. The exclusion of $1.37 < \eta < 1.52$ is due to the transition between barrel and end-cap calorimeter in this range, where the detector is not reliable.

4.2.2. Leptons

Electrons are also reconstructed by matching a track of the inner detector with energy clusters in the electromagnetic calorimeter. The particle identification working point 'Medium' (having an efficiency of ∼90%) and the isolation criterion 'Loose' [60] are used. In this analysis, electrons are only considered when they fulfill: $|\eta| < 2.47$, $|\eta| \notin \{1.37, 1.52\}$ and $p_T > 10$ GeV.

Muons are reconstructed by matching tracks in the inner detector with tracks in the muon spectrometer. The particle identification working point is 'Medium' and the isolation criterion is 'GradientLoose' [61]. Muons are furthermore required to have the characteristics: $|\eta| < 2.7$ and $p_T > 10$ GeV.

4.2.3. Jets

Anti-k_t ($R = 1.0$) jets with $|\eta| < 2$ and $p_T > 200$ GeV are considered in this analysis. The jets are trimmed with $f_{cut} = 5\%$ and $R_{sub} = 0.2$ as described in 3.4. The jet calibration is based on the track-assisted mass.

For the overlap removal discussed in section 4.3, Anti-$k_T(R = 0.4)$ jets are used. Only jets having $p_T > 25$, $|\eta| < 4.4$ and (JetVertexTagger, defined in reference [57]) $JVT > 0.59$ are considered.

4.3. Overlap removal

Due to the fact of parallel object reconstruction, it is possible, that the same energy deposition is used for the construction of several objects. For example photons and leptons also occur inside hadronic showering processes, prima facie resulting in double-counting of depositions, once as photon/lepton, once a jet. In order to correct for this behavior, an overlap removal is applied, removing overlapping objects aiming to only keep the true physical object in the collection. The procedure is as follows and in the following order. In parenthesis the aim of the rule is stated:

- Electrons, e, are discarded if $\Delta R_{e,\gamma} < 0.4$ for any photon, γ.
- Anti-$k_t(R = 0.4)$ jets, j, are discarded if $\Delta R_{j,\gamma} < 0.4$ for any photon, γ.
- Anti-$k_t(R = 0.4)$ jets, j, are discarded if $\Delta R_{j,l} < 0.2$ for any lepton, l.
- Leptons, l, are discarded if $\Delta R_{j,l} < \min(0.4, 0.04 + 10\ \text{GeV}/p_{T,l})$ for any Anti-$k_t(R = 0.4)$ jet, j . So non-prompt leptons resulting from decays of hadrons inside an hadronic shower are removed, while boosted leptons are kept.
- Muons, μ, are discarded if $\Delta R_{\mu,\gamma} < 0.4$ for any photon, γ.
- Anti-k_t $(R = 1.0)$ jets, J, are discarded if $\Delta R_{J,\gamma} < 1.0$ for any photon, γ.

This procedure deviates from a nominal overlap removal by the p_T dependent removal of leptons. This aims to allow for boosted leptons to remain in the selection: Assuming a semileptonic decay of the WW^* system, for heavy resonances, the angular separation between lepton and jet is small. It can be further assumed, that in this case the leptons carry significantly more p_T than leptons which are produced in the showering process. To remove the latter and not the former, the ΔR criterion is sensitive to $p_{T,l}$ such that for high p_T leptons a smaller angular separation is allowed. Despite the focus on the hadronic decay in this analysis, this procedure was chosen to ensure, comparability with later semileptonic analysis. The semileptonic analysis will in addition need a removal between leptons and large radius jets, such that leptons faking a large radius jet are removed. As a lepton veto is implemented for this study, this removal was omitted without loss of orthogonality.

4.4. Event selection

An event is considered in this analysis, if it fullfills several groups of criteria, defined below. These are called preselection, photon selection, diphoton selection, jet selection and vetoes, as well as an optimized $\Delta R_{\gamma\gamma}$ criterion discussed in chapter 4.6.

- Preselection includes exhaustively checking detector quality and good run list for data and requires exactly two loose photons matched to the primary vertex.
- The photon selection is passed if the two selected photons fulfill the tight identification criterion, as well as a relative p_T cut. For the invariant mass, $m_{\gamma\gamma}$, of the two photons γ_1, γ_2, whereby γ_1 is higher in p_T than γ_2, the relative p_T cut is fulfilled, if: $p_{T,\gamma_1}/m_{\gamma\gamma} > 0.35$ and $p_{T,\gamma_2}/m_{\gamma\gamma} > 0.25$. Both photons must also have a minimum p_T of 25 GeV.
- The diphoton selection requires 105 GeV $< m_{\gamma\gamma} <$ 160 GeV, as well as $m_{\gamma\gamma}$ to be inside (signal region) or outside (control region) the Higgs mass window. The Higgs mass window is defined as the interval $[(125.09 - 3.4)$ GeV, $(125.09 + 3.4)$ GeV$]$. This is the interval of $m_H \pm 2\sigma_\gamma$ with the photon mass resolution σ_γ.
- The jet selection requires the presence of at least one Anti-k_t ($R = 1.0$) jet, with $|\eta| < 2$ and $p_T > 200$ GeV.
- Vetoes on b-jets and leptons (electrons and muons) are in place. The b-tagger is $MV2c10$ [62] with a working point of 70 % b tagging efficiency).
- $\Delta R_{\gamma\gamma} < 0.75$, this cut is motivated in section 4.6.

The combination of all cuts, without but $\Delta R_{\gamma\gamma} < 0.75$ is in this thesis also referred to as the 'un-optimized selection'.

4.5. Continuum background estimation

For the optimization of the event selection the signal yield, s, and the background yield, b, are required. The optimization is described in chapter 4.6. For this purpose, however, an estimation of the background yield is necessary. As the decay $h \to \gamma\gamma$ should yield $m_{\gamma\gamma}$ close to m_h with high resolution the photon side of the event is used for background estimation. Consequently, the background consists of the MC generated $h \to \gamma\gamma$ samples described in chapter 3.3, as well as of a continuum background estimated from the control regions. For this estimation the diphoton mass spectrum in the sidebands was considered.

The sidebands are defined as the regions in data where 105 GeV $< m_{\gamma\gamma} <$ 160 GeV and $m_{\gamma\gamma} \notin [(125.09 - 3.4)$ GeV, $(125.09 + 3.4)$ GeV$]$). A fit is performed in order to interpolate from the distribution of the control region into the signal region. The integral of the fit function within the Higgs-boson mass window corresponds to the estimated background yield from the continuum background. For the fit a first order exponential was used ($f(m_{\gamma\gamma}) = \exp(a + b \cdot m_{\gamma\gamma})$).

Figure 4.4 shows the sideband fit after application of preselection, photon- diphoton- and jet selection with applied vetos (un-optimized event selection) for 22.7 fb^{-1}.

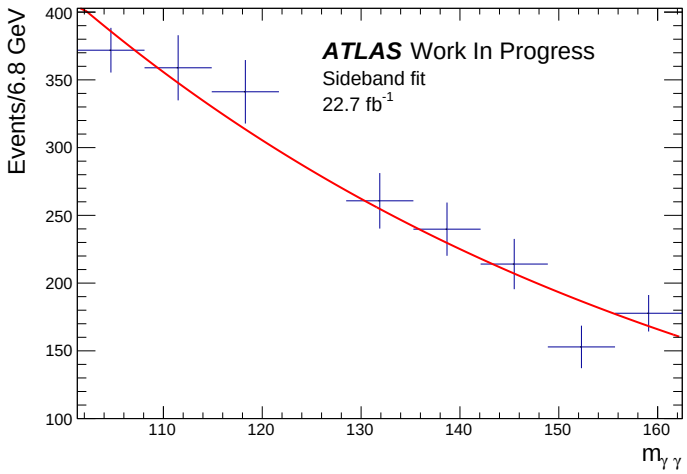

Figure 4.4.: Sideband fit for 22.7 fb^{-1} with the following cuts applied: Preselection, photon selection, diphoton selection, jet selection, vetoes. The integral of the fit inside the signal region approximates the yield of the continuum background. Fit details, integral within the signal region for the final fit are discussed in section 4.7. (The first and last bin are scaled up, as they lie partially outside the considered diphoton mass range and are therefore only partially filled.)

4.6. Optimization

The optimization was performed maximizing the value of the Cowan significance, $Z = \sqrt{2((s+b)\log(1+s/b)-s)}$ [63], for signal yield, s, directly counted from the MC signal sample and the background yield, b, which is the sum of the data-driven continuum background estimate and the MC background samples.

As the data sets were still being processed at this point of the analysis, the optimization was performed using 22.7 fb^{-1} of data, the event yields in data for the continuum background however were scaled up to estimate the significances for the full data set of 36.5 fb^{-1}.

A scan over several cut values for different parameters was performed in order to maximize the Cowan significance. In order to avoid significant correlations, one parameter with high seperation power belonging to the photon side ($\Delta R_{\gamma\gamma}$) and one belonging to the W-boson side (τ_{42}) of the topology were chosen. The $\Delta R_{\gamma\gamma}$ distribution is expected to be sensitive to the boost of the photons mother particle, which in turn is expected to be much higher for heavy resonances than for the majority of background processes. τ_{42}, on the other hand, is sensitive to the likelihood of the jet to be rather a 4-prong than a 2-prong jet as described in section 3.4. For the fully boosted topology, a 4-prong jet is expected for the 4 partons stemming from the two W-bosons. To allow also for 3-prong jets which could stem from the loss of one parton (either by errors in the reconstruction or due to a semi boosted topology with 3 partons in one, and 1 parton in a second large radius jet), τ_{42} instead of τ_{43} was chosen. In addition, previous studies have already observed, that τ_{42} has higher performance than τ_{43} in the context of tagging 4-prong jets [64]. For completion, a discussion of τ_{43} containing distributions is given in appendix A.2.

Furthermore, the procedure of interpolation assumes that the cut parameters are largely independent of $m_{\gamma\gamma}$. Only in this case, the upper and lower sideband of the $m_{\gamma\gamma}$ spectrum can be assumed to give valid estimations of the background in the signal region. The validity of this assumption can be seen in the corresponding distributions of the parameters.

Figures 4.5 and 4.6 show the normalized distributions of $\Delta R_{\gamma\gamma}$ and τ_{42}. Both indicate the separation power of the variables as well as the validity of the interpolation from both sidebands: The upper and lower sideband agree largely within their uncertainties. The expected correlation for $\Delta R_{\gamma\gamma}$, following $\Delta R \approx 2m/p_T$ (see chapter 3.4.3), predicts the lower sideband to be slightly shifted towards lower values of $\Delta R_{\gamma\gamma}$ than the upper sideband. The distribution also shows a small hint in favor of this expectation.

Figures 4.7 and 4.8 show the significance as a function of an upper limit cut on the parameter $\Delta R_{\gamma\gamma}$ and τ_{42} respectively.

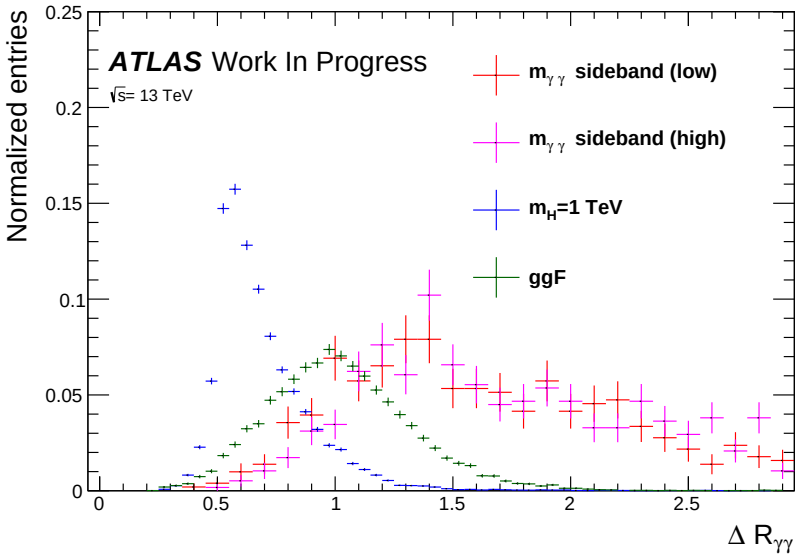

Figure 4.5.: Normalized distributions of $\Delta R_{\gamma\gamma}$, the sidebands are based on 22.7 fb^{-1}.

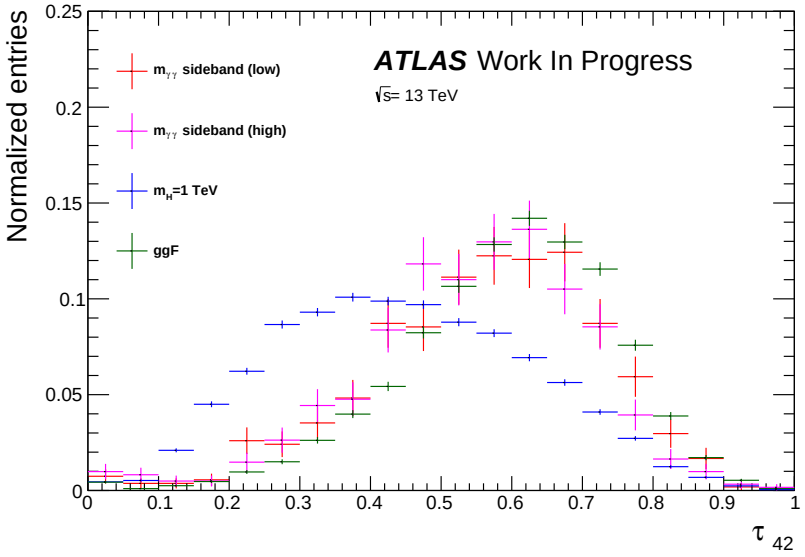

Figure 4.6.: Normalized distributions of τ_{42}, the sidebands are based on 22.7 fb^{-1}.

It follows that the cut on $\Delta R_{\gamma\gamma}$ should be given priority, due to higher significance. The cut value was chosen to be at 0.75 for two reasons: Firstly, the maximum at 0.685 appeared as a statistical fluctuation, such that it was decided to pick a point on the smoother slope. Secondly, a looser cut was preferred as this analysis has low statistics.

Figure 4.9 shows the significance as a function of an upper limit cut on the parameter τ_{42} after applying the cut $\Delta R(\gamma\gamma) < 0.75$. This optimization showed slight improvement in significance, but strongly limited the quality of the sideband fit due to too few events

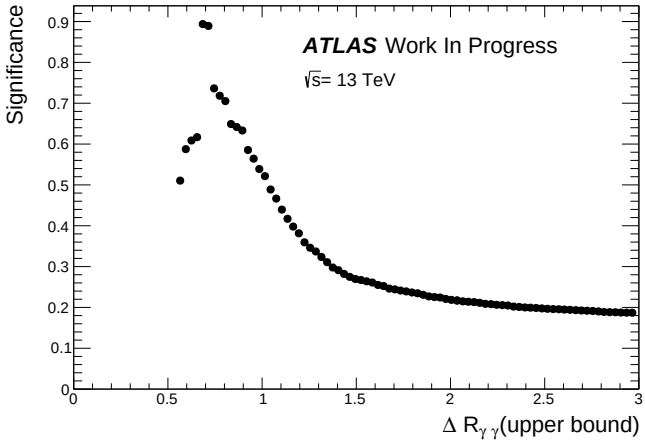

Figure 4.7.: Significance as a function of a cut $\Delta R_{\gamma\gamma} < X$, the sidebands are based on 22.7 fb^{-1}. For visual purposes, the error bars were omitted.

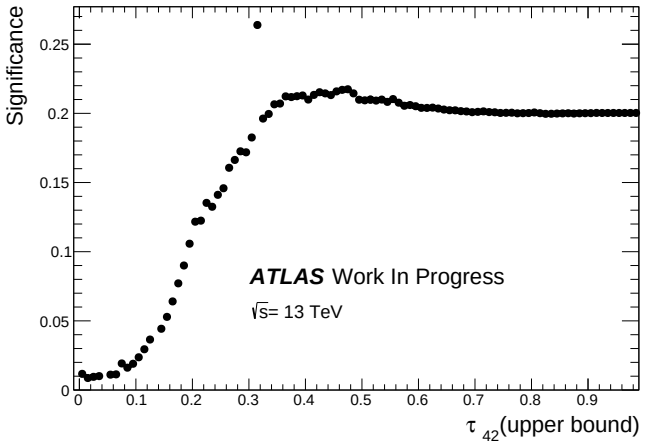

Figure 4.8.: Significance as a function of a cut $\tau_{42} < X$, the sidebands are based on 22.7 fb^{-1}. For visual purposes, the error bars were omitted. The isolated maximum could be traced back to a statistical fluctuation, when investigating the τ_{42} distribution with fine binning.

in the sidebands. The requirement for the fit was set to be a minimum of five events in the sidebands, which is the reason for no calculated significance below τ_{42} (upper bound) < 0.375 . As a result, τ_{42} was discarded as a variable to select events. For the same reason (limited statistics) no further cuts are implemented.

For all following sections, the complete dataset of 36.5 fb^{-1} was used.

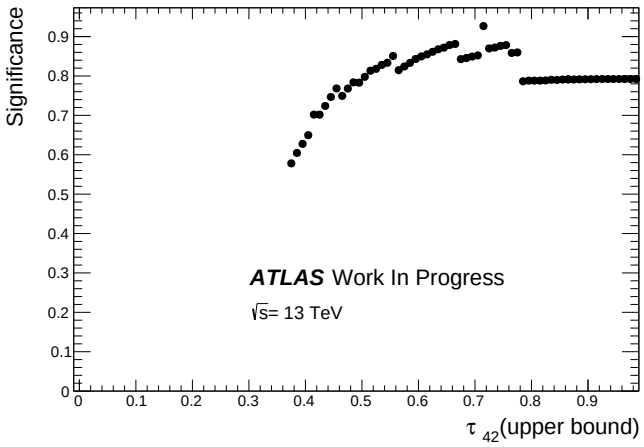

Figure 4.9.: Significance as a function of a cut $\tau_{42} < X$, given $\Delta R(\gamma\gamma) < 0.75$. The cut value, X, corresponding to the maximum significance is printed in the top left of the plot. For visual purposes, the error bars were omitted.

4.7. Cutflow and final fit

The cutflow for the complete set of selection criteria is shown for the sidebands, the MC background, non-resonant and resonant $m_H = 1$ TeV MC signals in table 4.1. In appendix A.1 every signal contribution is listed.

Table 4.1.: Cutflow for data, backgrounds, non-resonant signal and one resonant signal sample.

Cut	$m_{\gamma\gamma}$ sidebands	MC-bkg	non-resonant	$H \to hh$ ($m_H = 1$ TeV)
Preselection	33554432	2221.3 ±2.4	9.86 ±0.03	10.64 ±0.07
Photon sel	2249321	1601.5 ±2.1	7.26 ±0.03	8.28 ±0.06
Diphoton sel	28368	1445.6 ±2.0	6.41 ±0.03	7.47 ±0.06
Jet	358	32.00 ±0.29	2.99 ±0.02	5.06 ±0.05
Veto (b and lep)	338	26.86 ±0.26	1.94 ±0.02	3.18 ±0.04
Δ R	74	4.78 ±0.11	1.3 ±0.01	2.28 ±0.03

The final sideband fit was performed, using the complete dataset of 36.5 fb^{-1} and is shown in figure 4.10. The fit parameters are listed in table 4.2. For the fit quality, it is useful to investigate the number of degrees of freedom, NDf and the value of χ^2, defined as [65]

$$\chi^2 = \sum_{i=1}^{n} \frac{(O_i - E_i)^2}{E_i},$$

with the observed number of events in bin i denoted as O_i and the - based on the fit

- expected number E_i. There are two approaches to validate the fit quality. Firstly, it is useful to calculate χ^2/NDf and check, that the value is close to unity - which is a first sign of a valid fit. With $\chi^2/NDf = 1.14$ this is the case. Secondly, one can calculate the probability to see a χ^2 greater to the actually calculated χ^2 given the hypothesis - in this context the fit - is correct. This calculation is done by integrating the χ^2 distribution for a given value of NDf from 0 to the actually calculated χ^2 value. Performing this calculation yields a probability of about 64 % that $\chi^2 > 6.84$ assuming the fit is correct. This can be interpreted as a high fit quality, as usually only values of 5% or lower are considered reason to reject the fit results [65].

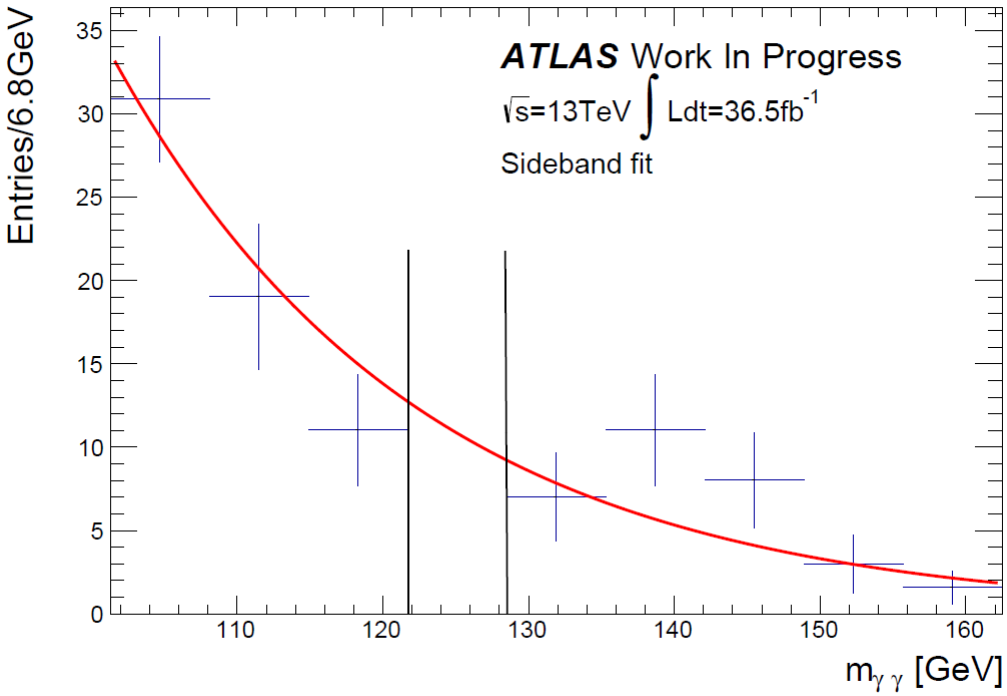

Figure 4.10.: Sideband fit for the complete data set with all cuts applied. The integral of the fit inside the signal region (depicted with vertical bars) approximates the yield of the continuum background.(The first and last bin are scaled up, as the boundaries of the histogram are not identical with the boundaries of the fit range.)

Calculation of the integral inside the Higgs mass window and the corresponding error propagation was performed as follows:

Let $f(a, b; m_{\gamma\gamma}) = \exp(a + b m_{\gamma\gamma})$ be the fit function and σ_a, σ_b, σ_{ab} be the uncertainties on a, b and the covariance between a and b respectively. Denote the Higgs mass window as the interval $[w_-, w_+]$. It follows for the integral of the fit function inside this interval: $F(a, b, w_-, w_+, m_{\gamma\gamma})$ (denoted simply as F):

Table 4.2.: Fit parameters for the final sideband fit. Used function: $f(x) = \exp(a+b\cdot x)$, fit quality parameters: $\chi^2 = 6.84$ and (degrees of freedom) $NDf = 6$. Fit range (with the exception of the Higgs mass window): 105 GeV $\leq m_{\gamma\gamma} \leq$ 160 GeV.

Parameter	Value	Correlation with a	Correlation with b
a	8.34 $\pm$0.76	1	-0.99
b	-0.0476 $\pm$0.0066	-0.99	1

$$F = \int_{w_-}^{w_+} f(a,b;m_{\gamma\gamma})dm_{\gamma\gamma} = \frac{1}{b}(\exp(a+bw_+) - \exp(a+bw_-)).$$

The error on F, denoted as σ_F, is based on the general error propagation formula:

$$\sigma_F^2 = \left(\frac{\partial F}{\partial a}\right)^2 \sigma_a^2 + \left(\frac{\partial F}{\partial b}\right)^2 \sigma_b^2 + 2\frac{\partial F}{\partial a}\frac{\partial F}{\partial b}\sigma_{ab}$$

and is consequently given as:

$$\begin{aligned}\sigma_F^2 = F^2\sigma_a^2 &+ \left(-\frac{F}{b} + \frac{w_+\exp(a+bw_+) - w_-\exp(a+bw_-)}{b}\right)^2 \sigma_b^2 \\ &+2F\left(-\frac{F}{b} + \frac{w_+\exp(a+bw_+) - w_-\exp(a+bw_-)}{b}\right)\sigma_{ab}\end{aligned}$$

Based on the 74 events in the sidebands, the estimated data-driven background contribution is 10.89 ± 1.22 (only considering statistical uncertainties). Due to the strong anticorrelation of the fit parameters, the error is approximately 12%. However more aggressive cuts would lead to the procedure of performing a fit into the signal region unfeasible, as the statistical uncertainty would increase dramatically.

Event yields for MC backgrounds and signal are listed and discussed in the following section 4.8.

4.8. Event yields for signal and background estimation

Table 4.3 shows the event yields for the various contributions: continuum background, every MC background and MC signal for non-resonant and resonant (500 GeV $\leq m_H \leq$ 3 TeV). The data-driven background estimate is the dominant background. The ggF contribution however is only about 60% smaller. Only statistical uncertainties are quoted.

Table 4.3.: Yields for various contributions after event selection, only considering statistical uncertainties.

Channel	Event yield
Cont-Bkg	10.89 ± 1.22
ggF	3.43 ± 0.09
VBF	0.68 ± 0.04
WH	0.32 ± 0.02
ZH	0.20 ± 0.01
$t\bar{t}H$	0.17 ± 0.02
Bkg_{all}	15.69 ± 1.23
non-reso	1.30 ± 0.01
$m_H = 500$ GeV	0.02 ± 0.01
$m_H = 750$ GeV	0.34 ± 0.01
$m_H = 1000$ GeV	2.28 ± 0.03
$m_H = 1500$ GeV	4.77 ± 0.03
$m_H = 2000$ GeV	6.02 ± 0.04
$m_H = 2500$ GeV	5.40 ± 0.04
$m_H = 3000$ GeV	3.82 ± 0.03

In addition to finalizing the event selection it is necessary to finalize the background estimates, before the signal region can be unblinded (i.e. data events inside the Higgs mass window can be analyzed), which in this context amounts to counting the observed events in the signal region, that pass the event selection. The next section 4.9 will discuss the systematic uncertainties, which are a relevant part of the background (and signal) estimation and therefore a prerequisite to unblinding.

4.9. Systematic uncertainties

Next to statistical uncertainties, also systematic uncertainties were considered. Systematic variations were applied for every MC sample to account for the imperfect simulation of data. Furthermore, the process of performing a sideband fit for determining the continuum

background is also subject to systematic uncertainties. Due to time constraints, a subset of systematic uncertainties was considered, particularly containing those, which are expected to be the most important for this analysis.

The various systematic uncertainties are described in section 4.9.1, the most significant applied systematic uncertainties are listed in table 4.4, while all applied systematic uncertainties are presented in the appendix. Further systematic uncertainties, that were neglected in this analysis due to time constraints are described in section 4.9.2.

4.9.1. Applied systematic uncertainties

For the data-driven estimation of the continuum background three systematic uncertainties were considered. In each case the effect on the predicted event yield was symmetrized: When a fluctuation changes the event yield Y to $Y + \Delta Y$ an uncertainty of $\pm\Delta Y$ was applied.

- Variation of the fit range: For the calculations the fit range was set to be 105 GeV $< m_{\gamma\gamma} <$ 160 GeV. To estimate the systematic uncertainty, the fit range was decreased to 110 GeV $< m_{\gamma\gamma} <$ 155 GeV.
- Variation of the signal window: The signal window was increased by 3.4 GeV from 121.69 GeV $< m_{\gamma\gamma} <$ 128.49 GeV ($m_h \pm 2\sigma_\gamma$) to 119.99 GeV $< m_{\gamma\gamma} <$ 130.19 GeV ($m_h \pm 3\sigma_\gamma$).
- Modification of the functional form of the fit: Instead of fitting a first order exponential function $f(x) = \exp(a + b \cdot x)$, a second order exponential function $f(x) = \exp(a + b \cdot x + c \cdot x^2)$ was used.

For the MC background and signal samples, the following systematic uncertainties were considered:

- Theory uncertainty on production cross section and branching ratio as listed in reference [16]: While for background both uncertainties play a role, for signal only the branching ratio uncertainty is relevant, as the production cross section was assumed to be exactly 1 pb. A 1σ variation was considered.
- Uncertainties on the jet energy scale (JES) and jet energy resolution (JER) were applied [66]. A 1σ variation was considered.
- A scale factor for the photon ID efficiency (PID) was taken into account [67]. A 1σ variation was considered.

- An uncertainty on the luminosity of 4.1 % was considered.
- The used signal samples were produced using fast simulation. A systematic uncertainty connected to using fast simulation was estimated by comparing one full simulation sample and one fast simulation sample of one resonant mass point ($m_H = 1.5$ TeV). The corresponding difference in the event yield was again symmetrized.

Table 4.4.: Applied systematic uncertainties and their effect on the event yield for the various contributions.

Systematic Uncertainty	Effect on yield (up, down in %)	Contribution affected
Luminosity	(+4.1, -4.1)	MC
Fit-window	(+13.8, -13.8)	cont. bkg
Sig-window	(+20.1, -20.1)	cont. bkg
Functional form fit	(7.4, -7.4)	cont. bkg
Theo. $\sigma \cdot BR$	(+4.9, -6.9)	MC Bkg
Theo. BR	(+1.8, -1.8)	MC Sig
ATLfast/Fullsim	(+9.9, -9.9)	MC Sig
PID	(+2.1, -2.1)	MC Bkg
	(+2.3, -2.2)	MC Sig
JER	(+0.7, -0.9)	MC Bkg
	(+0.4, -0.5)	MC Sig
JES	(+0.8, -0.8)	MC Bkg
	(+0.8, -0.8)	MC Sig

4.9.2. Other systematic uncertainties

For further improvements of this analysis, the following systematic uncertainties should also be considered:

- Photon energy resolution and photon energy scale uncertainties [67]: As photons are an integral part of this analysis, these are expected to be the most relevant systematic, that was not applied.
- Lepton identification, energy scale and energy resolution uncertainties: This aims to account for detector resolution, uncertainties in the scale factors of electromagnetic calorimeter and scintillator response and temperature effects. In addition uncertainties on the reconstruction in the inner detector have to be considered. These uncertainties play a role, as a lepton veto is applied.
- b-tagger uncertainties: As a b-veto is applied in this analysis, the uncertainty on the b-tagger influences the event yield and should therefore be analyzed.
- Uncertainties on the pile-up reweighting of MC: Pile-up reweighting takes the effect of additional collisions and interactions into account, which are not tied to the primary interaction in question.
- Uncertainty on spurious signal, following the procedure described in [68]: A signal-plus-background fit is performed for various signal hypotheses in a background-only sample. The resulting 'false' signal yield is taken as an uncertainty, as it is only an effect of the background modeling.

5. Results

This chapter describes the final background estimation, analysis of data inside the signal region 5.1 and consequently limits on di-Higgs production 5.2.

5.1. Final cutflow and event yields

Following table 4.3 and table 4.4 the final background estimation can be calculated. The continuum background estimation amounts to 10.89 ± 1.22 (stat) ± 4.50 (syst) events, while the MC background SM $h \to \gamma\gamma$ amounts to 4.8 ± 0.11 (stat) $^{+0.41}_{-0.52}$ (syst) events. The total background estimation, n_{bkg}, is therefore:

$$n_{bkg} = 15.69 \pm 1.23 \text{ (stat)} \, ^{+4.52}_{-4.53} \text{ (syst)}.$$

With both the event selection and the background estimation fixed, the event yield in the signal region can be analyzed. Table 5.1 shows the cutflow for the observed events in data, showing 12 events after applying the complete event selection. Less events are observed than expected in the background-only hypothesis, however the number of observed events is consistent with the expected background yields within uncertainties.

Table 5.1.: Cutflow table for data events in the signal region. After all selection criteria, 12 events remain in the signal region.

cut	data
Preselection	33554432
Photon sel	2249321
Diphoton sel	73949
Jet	654
Veto (b and lep)	611
Δ R	12

5.2. Limits

As no excess has been found, an upper limit scan was performed, utilizing the HistFitter package [69]. Table 5.2 shows the upper limit for the non-resonant production mode, while the limits for the resonant production modes are depicted in Figures 5.1 (considering only statistical uncertainties) and 5.2 (considering statistical and systematical uncertainties). The effect of the considered systematic uncertainties on the upper limit is at about 10 % for the various channels. The observed limit is within 1σ of the expected limit.

Table 5.2.: Observed and expected upper limits for non-resonant production, with and without taking systematic uncertainties into account

Nonresonant Upper limit on $\sigma \cdot BR$ [pb]	mean	$+1\sigma$	$+2\sigma$	-1σ	-2σ
Observed	6.36				
Expected	8.26	12.33	18.14	5.77	4.16
Observed (stat-only)	5.51				
Expected (stat-only)	7.57	11.32	16.58	5.22	3.75

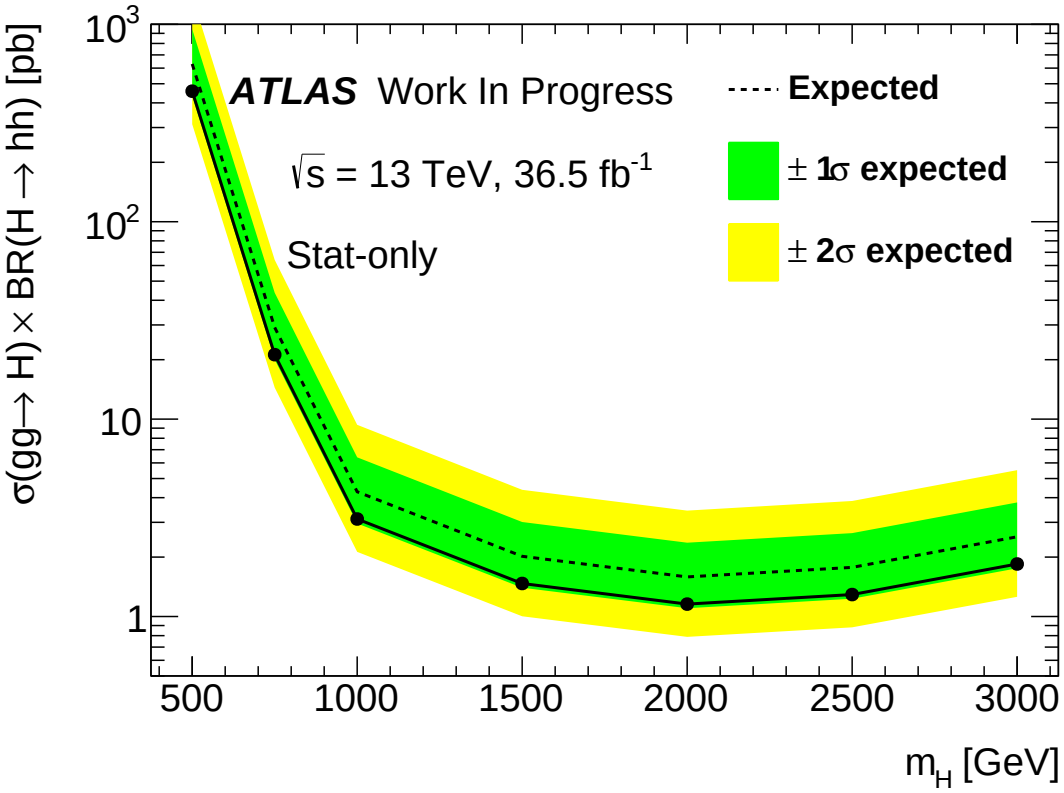

Figure 5.1.: Results of the upper limit scan for various hypothetical values of m_H. Only statistical uncertainties are taken into account.

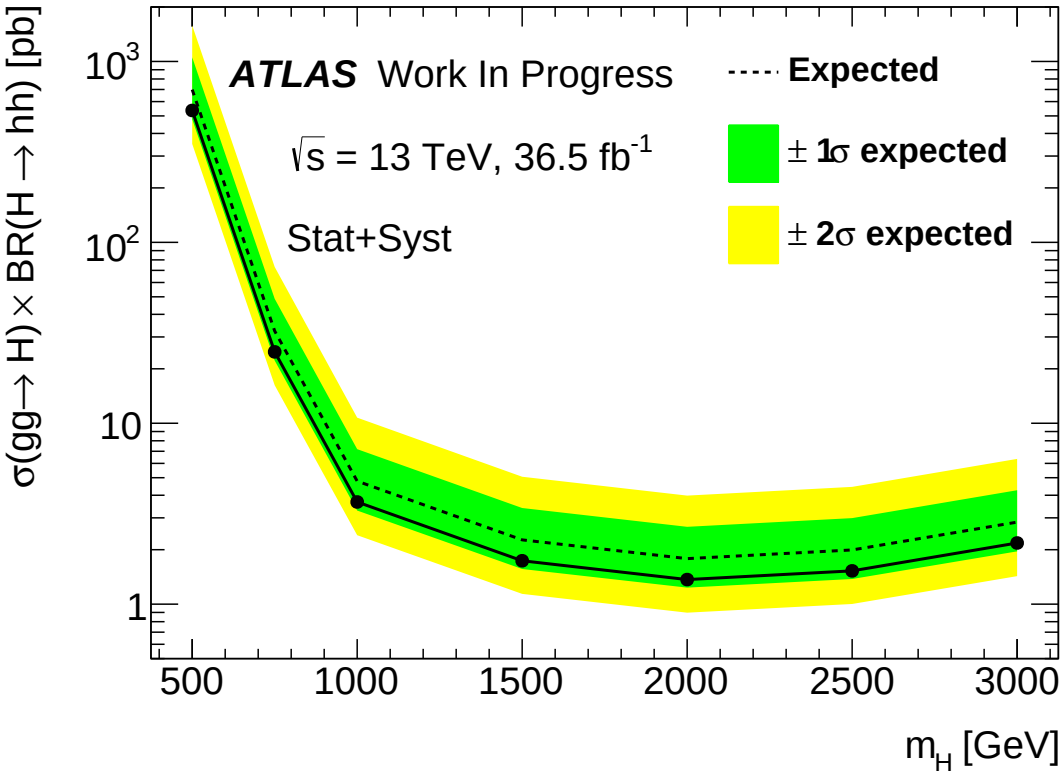

Figure 5.2.: Results of the upper limit scan for various hypothetical values of m_H. Statistical and systematical uncertainties are taken into account.

For the limits on the resonant di-Higgs production, two aspects have to be noted. Firstly, mass points below 500 GeV, namely 260, 300 and 400 GeV are not shown. However, as already indicated by the sharp rise in the upper limit for 500 GeV, this analysis exhibits little significance in this mass range. Below 500 GeV, the fitting procedure is unstable, as too few signal events pass the selection criteria. The reason for this behavior is directly connected to the topology of this channel: Below 500 GeV, the reconstruction with at least one large radius jet is not feasible, especially because large radius jets are only well understood for $p_T \geq 200$ GeV and therefore a $p_{T,jet}$ cut of 200 GeV is applied. This effect also explains the increase of sensitivity and decrease of the upper limit for higher mass points up to 2 TeV. Secondly, another increase in the upper limit can be seen above 2 TeV. This behavior can be connected to the limited resolution of the detector in identifying photons. The photon side will also exhibit a significant boost for high mass resonances, which will decrease the radial distance between the photons. However, further study is necessary to ascertain the validity of this hypothesis.

6. Conclusion and outlook

As no evidence for di-Higgs production was found, limits on the production cross section for non-resonant production as well as for a spectrum of mass points for heavy resonances were set. The limits are at least on the order of pb and therefore two orders of magnitude higher than the SM prediction for di-Higgs production. A comparison to previous studies is difficult, because as of now (for $\sqrt{s} = 13$ TeV), the $H \to hh \to \gamma\gamma WW^*$ channel was only studied for mass points of $m_H \leq 500$ GeV. Comparing the limit for $m_H = 500$ GeV with the results in [29], depicted in figure 2.9 in chapter 2, shows, that the limit calculated here is about one order of magnitude higher. For the boosted regime, which was the focus of the study presented here, a comparison is not yet possible.

However, the limiting factor of this analysis is low statistics. The data-driven estimate of the continuum background is the major contributor to the background and even more so to the uncertainties on the background yields (see section 5.1). Furthermore, the procedure of performing sideband fits for estimation requires looser cuts, than would otherwise be possible: The quality and feasibility of the fit is directly tied to the number of events passing the cuts. More statistics could not only allow for better fits reducing uncertainty on the continuum background but would also leave room for improvement when trying to suppress $h \to \gamma\gamma$ background, as then additional cuts focusing on the WW^* side of the topology can be set. In this analysis only one parameter could be optimized on ($\Delta R_{\gamma\gamma}$), later studies can aim to utilize for example substructure variables on the large radius jets as well, some suitable variables are listed and discussed in appendix A.2. When trying to add further cuts to the event selection without increasing the dataset, it is also possible to estimate the continuum background yield by not fitting sidebands into the signal region, but rather into a control region. This is however far from ideal, as it introduces new assumptions (i.e. that distributions in signal region and control region are largely identical).

Next to using more data, further studies along the lines of this analysis should increase the number of considered systematic uncertainties, as several could not be regarded due to time constraints.

For low statistics searches, like the one presented here, it is crucial to combine every channel available. One recommendation to combine this boosted analysis with an analysis focusing on low mass resonances is explained in section A.1 in the appendix.

With data from the high luminosity LHC, the combination of channels can be expected to be sensitive to a BSM increase in the non-resonant di-Higgs production as well as to the presence of heavy resonances. Studies looking at heavy resonances and boosted final states will become increasingly important. The analysis presented here can be re-done with a larger dataset in the future, in the hope of improving our understanding of the Higgs-sector.

A. Appendix

A.1. Study on combining analysis

The study presented here only investigated one particular decay channel of di-Higgs production. Furthermore in this channel, the analysis focused on one regime, namely the heavy resonant mass points at 0.5 TeV $\leq m_H \leq$ 3 TeV. In order to be sufficiently sensitive to BSM effects, every available regime of every available channel should be combined. The following presents one investigation as to how to combine a boosted with a resolved analysis of $hh \to \gamma\gamma WW^*$ with hadronically decaying W-bosons. The discussion focuses one the resonant di-Higgs production.

Two aspects are crucial when combining two analysis:

- The orthogonality of the studies must be ensured.
- No sensitivity should be discarded.

A resolved analysis, utilizing small radius jets to reconstruct each parton, is mostly sensitive to low resonance mass regions with $m_H < 750$ GeV. A boosted analysis only becomes reasonably sensitive at high mass points with roughly $m_H \geq 1$ TeV as explained in section 4.1. A naive approach is therefore to find a cut value in m_H below which a resolved and above which a boosted analysis is performed. This would ensure orthogonality, but violate the second aspect: Every sensitivity of the resolved analysis for high mass points as well as every sensitivity of the boosted analysis for low mass points is lost.

However, a refined approach can be investigated: Combine for a cut and count analysis the events which pass the event selection of the resolved analysis (R) with those, which pass the event selection of the boosted, but not of the resolved analysis ($B!R$). Similarly the events passing the boosted selection (B) can be combined with those passing the resolved but not the boosted selection ($R!B$).

As now R and $B!R$ as well as B and $R!B$ are orthogonal to each other, in both combinations every available event is used. With this modification, one can now investigate a possible cut-off value in m_H, such that below the value the events are counted which

are in the categories R or $B!R$ and above which the events are counted, which are in the categories B or $R!B$. To find a cut-off value the distribution of significance in dependence of m_H for the two combinations of categories is investigated.

The event selection of section 4.4 is used to define the category B, while for the category R, the same selection is modified: The requirement of one large radius jet and the cut on $\Delta R_{\gamma\gamma}$ are replaced by the requirement of at least 3 small radius jets (Anti-$k_T(R = 0.4)$) with $\eta < 2.5$ and $p_T > 25$ GeV.

The following study uses the continuum background estimate as described in section 4.5 and 22.66 fb^{-1} of data - scaled up to the full dataset, to get expected significances for the final analysis.

Using the significance defined in section 4.6, figure A.1 shows the the significance in dependence of m_H for the two combinations, while figure A.2 shows the significances of every category and combination thereof.

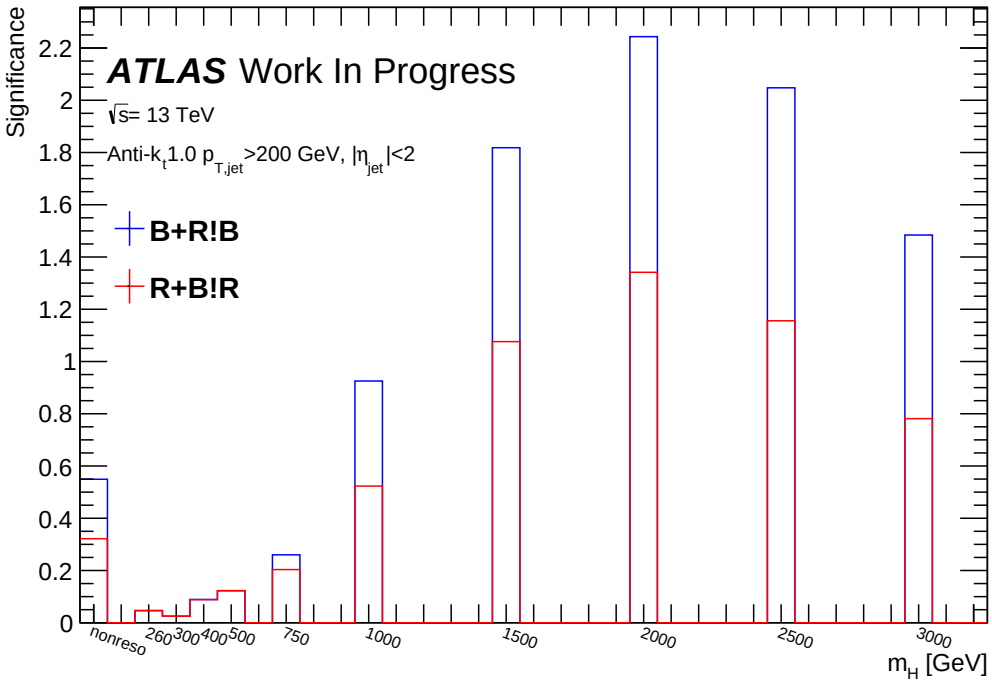

Figure A.1.: Significances for the combinations 'Boosted and Resolved but not Boosted' (B+R!B) and 'Resolved and Boosted but not Resolved' (R+B!R) for several signal contributions. The significance of B+R!B is always higher or equal than the significance of R+B!R.

Figure A.1 clearly shows, that the combination B and $R!B$ never results in less significance than the combination R and $B!R$. Consequently no cut-off value needs to be chosen.

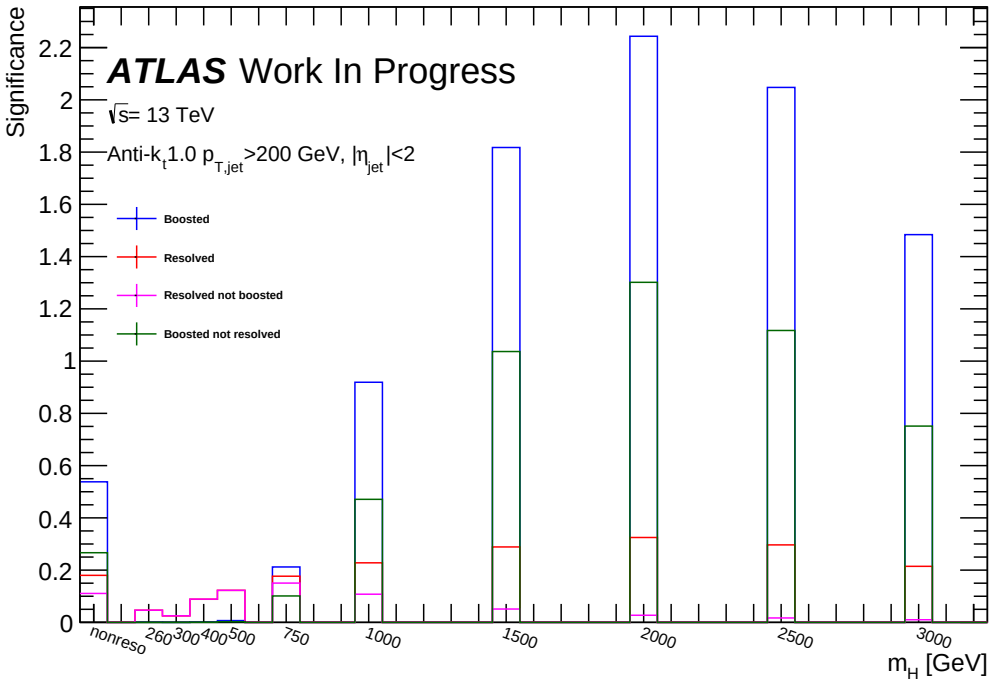

Figure A.2.: Significances for the selection criteria 'Boosted' and 'Resolved' and their combinations 'Boosted but not Resolved' and 'Resolved but not Boosted'. For low mass points, the boosted category yields no significance, consequently 'Resolved' and 'Resolved and not Boosted' are identical. Beginning at $m_H = 0.75$ TeV, the boosted outperforms the resolved category.

Instead the combination B and $R!B$ should be used for every investigated di-Higgs signal. The reason for the fact, that the combination B and $R!B$ outperforms R and $B!R$ can be seen in the particular distributions in figure A.2: The boosted category has almost no sensitivity for low mass points, such that vetoing large radius jets with $p_T \geq 200$ GeV does not reduce the significance of the resolved analysis. Consequently the sensitivity of R is completely covered by $R!B$.

Finally it can be noted, that the shape of the sensitivity for the boosted analysis largely coincides with the inverted distribution of the upper limits, described in section 5.2. The reasons can be expected to be identical: The higher the significance, the better the expected upper limit. However, the fact that the boosted analysis has higher significance at $m_H = 260$ GeV than at $m_H = 300$ GeV can not be explained with the arguments put forward in sec. 5.2. Whether a random fluctuation is the reason for this behavior or rather an effect tied to the very small phase space of a $m_H = 260$ GeV heavy Higgs-boson

decaying into two 125 GeV SM Higgs-bosons, was not investigated further, as it was not the primary focus of this analysis.

Nonetheless it can be concluded from this study, that for the combination of the boosted with the resolved regime in the channel $hh \to \gamma\gamma W_{had} W^*_{had}$, it is promising to combine events passing the boosted event selection, described in section 4.4 with the events passing the resolved but not the boosted selection.

It must be noted however, that this study compared the optimized boosted event selection with a basic selection for the resolved analysis. As a corresponding resolved analysis is still ongoing at this point in time, no comparison with a final event selection was possible. The argument put forward in this study, namely, that the very low significance of the boosted selection for low mass points, results in $B + R!B$ outperforming $B + R!B$, holds nonetheless: As the resolved analysis focuses on low mass points, further optimization will increase the significance of R and $R!B$ simultaneously, such that the proposed combination $B + R!B$ is still expected to outperform its counterpart.

A.2. Investigated parameters

Next to the parameters discussed in section 4.6, several other parameters were investigated. A few of which are listed in this appendix. All are on the basis of 22.7 fb^{-1} and show the two sidebands, the ggF contribution as well as the resonant signal for $m_H = 1$ TeV. For all plots the un-optimized event selection was used (all cuts except for the ΔR cut were applied). The investigation was subdivided into three parts:

- Investigation of parameters focusing on the WW^* side of the topology
- Investigation of parameters focusing on the $\gamma\gamma$ side of the topology
- Investigation of parameters focusing on the relation between the two sides

An example of a parameter connected to the WW^* side is the N-subjettiness variable τ_{43}, depicted in figure A.3. It noticeably performs worse than τ_{43} as already described in section 4.6. As the signal and background distributions in τ_{43} largely agree within their uncertainties, this variable was not considered further.

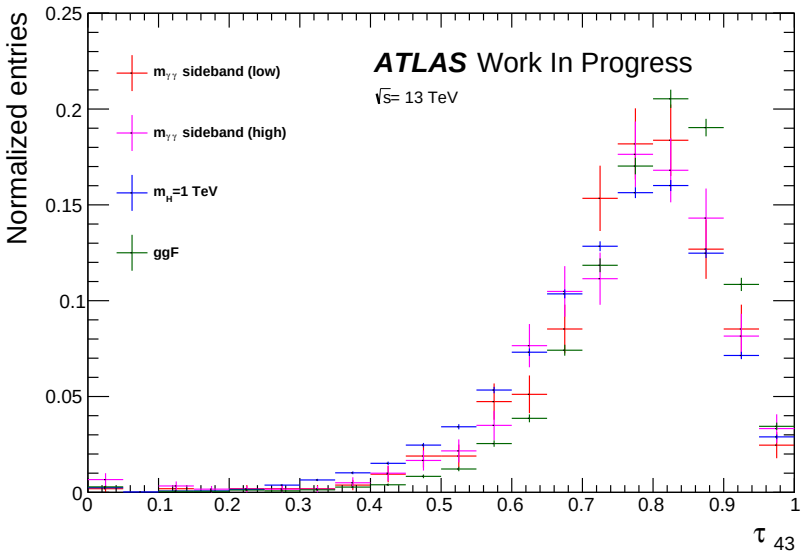

Figure A.3.: Distributions of τ_{43}. No separation power is noticeable.

On the $\gamma\gamma$ side of the topology, it is possible to investigate the transverse momentum of the diphoton. This variable should be sensitive to the mass of the resonance: Heavy resonances should exhibit a higher $p_{T,\gamma\gamma}$ than background processes. Figure A.4 shows the corresponding distributions. A clear separation power is noticeable, however, the signal distribution is highly sensitive to the value of m_H of the resonant production. This

sensitivity can be a difficulty when optimizing on only one mass point, as the optimization can then not be expected to perform well for other mass points. Furthermore, a significant correlation with $\Delta R_{\gamma\gamma}$ is to be expected (as $\Delta R_{\gamma\gamma}$ is also connected to the initial p_T as discussed in section 4.6.

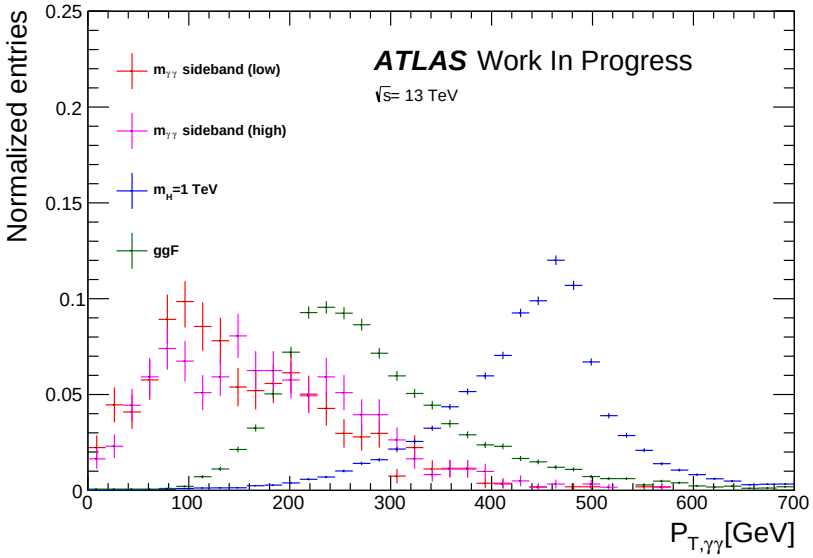

Figure A.4.: Distributions of $P_{T,\gamma\gamma}$. Strong separation power is noticeable. This variable is expected to be sensitive to the initial mass of a heavy resonance ($p_{T,\gamma\gamma} \approx m_H/2$).

When comparing the two sides of the topology, the following two variables were investigated: The ratio of p_T and the angular separation between the two sides. Here, a fully boosted topology was assumed and the p_T-leading jet was assumed to represent the WW^* side.

Figure A.5 shows the angular separation. Next to a small excess of background in the tails of the distribution, no separation power can be seen. This validates however, the back-to-back production of jet and diphoton.

Figure A.6 shows the ratio $p_{T,\gamma\gamma}/p_{T,J}$. While a certain separation power is noticeable, the signal distribution shows clear sings of the WW^* side having less p_T. This is to be expected, as only the leading jet was taken into account, which only is valid for the fully boosted topology. However, here can with sufficient statistics also a cut be implemented.

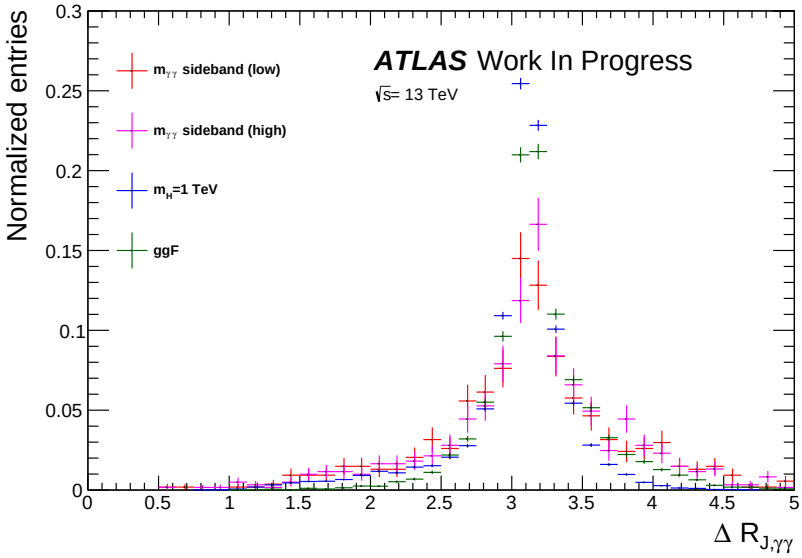

Figure A.5.: Distributions of $\Delta R_{J,\gamma\gamma}$. No separation power is noticeable.

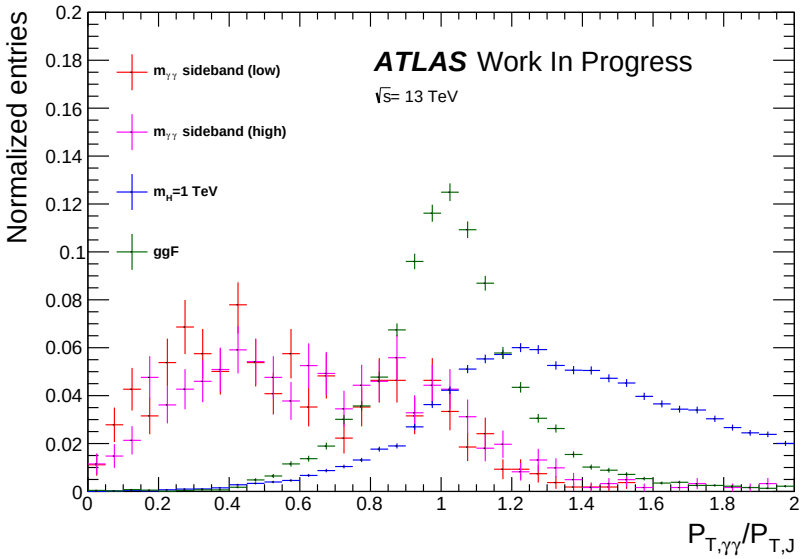

Figure A.6.: Distributions of $p_{T,\gamma\gamma}/p_{T,J}$. Separation power is noticeable. The excess of signal for high values is due to the fact, that only the leading jet was considered, ignoring semi-boosted topologies.

A.3. Cutflow table and event yield

Table A.1 shows the cutflow of all resonant signal samples, while table A.2 shows event yields for all investigated channels, including data.

Table A.1.: Cutflow for resonant signal samples. Uncertainties on the final yields are shown in table A.2. Sample notation follows the convention: XA corresponds to $m_H = A$ TeV.

Cut	X500	X750	X1000	X1500	X2000	X2500	X3000
Preselection	9.08	6.71	10.64	11.32	11.46	9.8	7.36
Photon sel	6.49	5.07	8.28	8.99	9.14	7.67	5.3
Diphoton sel	5.67	4.52	7.47	8.18	8.32	6.97	4.76
Jet	0.54	2.02	5.06	7.01	7.66	6.52	4.5
Veto (b and lep)	0.28	1.17	3.18	5.14	6.17	5.47	3.86
Δ R	0.02	0.34	2.28	4.77	6.02	5.4	3.82

Table A.2.: Yields for the various contributions after event selection. Sample notation follows the convention: XA corresponds to $m_H = A$ TeV. Only statistical errors are shown.

Channel	Yield
Data	12.0 ± 3.46
Cont-Bkg	10.89 ± 1.22
ggF	3.43 ± 0.09
VBF	0.68 ± 0.04
WH	0.32 ± 0.02
ZH	0.20 ± 0.01
$t\bar{t}H$	0.17 ± 0.02
non-reso	1.30 ± 0.01
X500	0.02 ± 0.01
X750	0.34 ± 0.01
X1000	2.28 ± 0.03
X1500	4.77 ± 0.03
X2000	6.02 ± 0.04
X2500	5.40 ± 0.04
X3000	3.82 ± 0.03

A.4. Significance scans - including error bars

The following figures show again the significance scans from section 4.6. For visual purposes, the error bars were omitted in the discussion. The following plots, however, include the error bars.

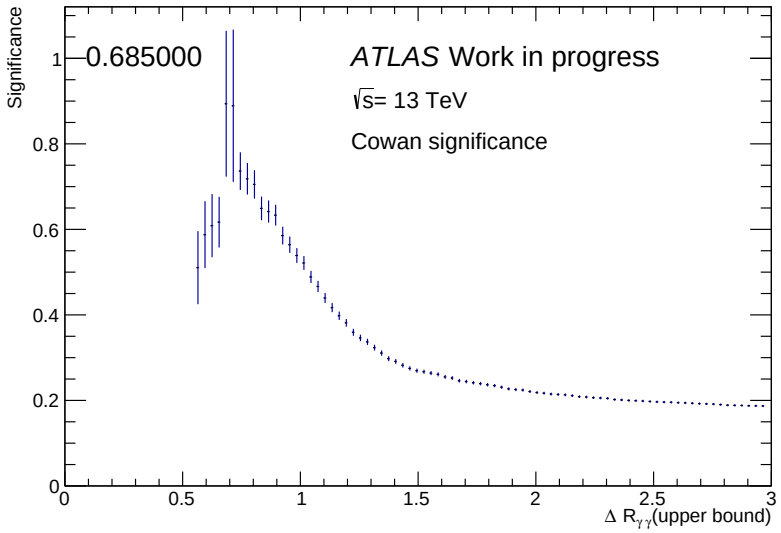

Figure A.7.: Significance scan of chapter 4.6: Scan for optimal cut value on $\Delta R_{\gamma\gamma}$. Cut value yielding the highest significance is printed in the top left corner.

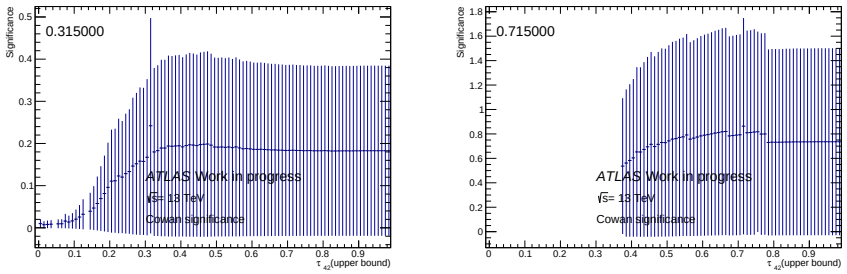

Figure A.8.: Significance scan of chapter 4.6: Scan for optimal cut value on τ_{42} (left) and scan given $\Delta R_{\gamma\gamma} < 0.75$ (right). Cut value yielding the highest significance is printed in the top left corner.

A.5. MC samples

Table A.3.: Signal samples for non-resonant production and resonant productions for several m_H points.

Mass point m_H	Signal sample name
non-resonant	mc15_13TeV.342621.aMcAtNloHerwigppEvtGen_UEEE5_CTEQ6L1 _CT10ME_hh_yyWW.merge.AOD.e4419_a766_a821_r7676
260 GeV	mc15_13TeV.343756.aMcAtNloHerwigppEvtGen_UEEE5_CTEQ6L1 _CT10ME_Xhh_m260_yyWW.merge.AOD.e5153_a766_a821_r7676
300 GeV	mc15_13TeV.343758.aMcAtNloHerwigppEvtGen_UEEE5_CTEQ6L1 _CT10ME_Xhh_m300_yyWW.merge.AOD.e5153_a766_a821_r7676
400 GeV	mc15_13TeV.343761.aMcAtNloHerwigppEvtGen_UEEE5_CTEQ6L1 _CT10ME_Xhh_m400_yyWW.merge.AOD.e5153_a766_a821_r7676
500 GeV	mc15_13TeV.343763.aMcAtNloHerwigppEvtGen_UEEE5_CTEQ6L1 _CT10ME_Xhh_m500_yyWW.merge.AOD.e5153_a766_a821_r7676
750 GeV	mc15_13TeV.343818.aMcAtNloHerwigppEvtGen_UEEE5_CTEQ6L1 _CT10ME_Xhh_m750_yyWW.merge.AOD.e5153_a766_a821_r7676
1000 GeV	mc15_13TeV.343819.aMcAtNloHerwigppEvtGen_UEEE5_CTEQ6L1 _CT10ME_Xhh_m1000_yyWW.merge.AOD.e5153_a766_a821_r7676
1500 GeV	mc15_13TeV.343820.aMcAtNloHerwigppEvtGen_UEEE5_CTEQ6L1 _CT10ME_Xhh_m1500_yyWW.merge.AOD.e5153_a766_a821_r7676
2000 GeV	mc15_13TeV.343821.aMcAtNloHerwigppEvtGen_UEEE5_CTEQ6L1 _CT10ME_Xhh_m2000_yyWW.merge.AOD.e5153_a766_a821_r7676
2500 GeV	mc15_13TeV.343822.aMcAtNloHerwigppEvtGen_UEEE5_CTEQ6L1 _CT10ME_Xhh_m2500_yyWW.merge.AOD.e5153_a766_a821_r7676
3000 GeV	mc15_13TeV.343823.aMcAtNloHerwigppEvtGen_UEEE5_CTEQ6L1 _CT10ME_Xhh_m3000_yyWW.merge.AOD.e5153_a766_a821_r7676
1500 GeV (fullsim)	mc15_13TeV.343820.aMcAtNloHerwigppEvtGen_UEEE5_CTEQ6L1 _CT10ME_Xhh_m1500_yyWW.merge.AOD.e5153_s2726_r7772_r7676

Table A.4.: Background SM $h \to \gamma\gamma$ samples.

Channel	Background sample name
ggH	mc15_13TeV.341000.PowhegPythia8EvtGen_CT10_AZNLOCTEQ6L1 _ggH125_gamgam.merge.AOD.e3806_s2984_r8585_r7676
VBF	mc15_13TeV.341001.PowhegPythia8EvtGen_CT10_AZNLOCTEQ6L1 _VBFH125_gamgam.merge.AOD.e3806_s2608_r7772_r7676
ZH	mc15_13TeV.341068.Pythia8EvtGen_A14NNPDF23LO _ZH125_gamgam.merge.AOD.e3796_s2608_s2183_r7772_r7676
WH	mc15_13TeV.341067.Pythia8EvtGen_A14NNPDF23LO _WH125_gamgam.merge.AOD.e3796_s2608_s2183_r7772_r7676
ttH	mc15_13TeV.341069.Pythia8EvtGen_A14NNPDF23LO _ttH125_gamgam.merge.AOD.e3796_s2608_s2183_r7772_r7676

Bibliography

[1] K. O. et al. (Particle Data Group), *2014 Review of Particle Physics*, Chin. Phys. **C38**, 090001 (2014)

[2] S. Glashow, *Partial Symmetries of Weak Interactions*, Nucl. Phys. **22**, 579 (1961)

[3] S. Weinberg, *A Model of Leptons*, Phys. Rev. Lett. **19**, 1264 (1967)

[4] J. I. S. Glashow, L. Maiani, *Weak Interactions with Lepton-Hadron Symmetry*, Phys. Rev. D **2**, 1285 (1970)

[5] A. Salam, *Weak and Electromagnetic Interactions*, Almqvist & Wiksell, Stockholm, nobel symposium 8 edition (1968)

[6] F. Englert, R. Brout, *Broken symmetry and the mass of gauge vector mesons*, Phys. Rev. Lett. **13(9)**, 321 (1964)

[7] P. Higgs, *Broken symmetries and the masses of gauge bosons*, Phys. Rev. Lett. **13(16)**, 508 (1964)

[8] S. C. et al., *Observation of a new boson at a mass of 125 GeV with the CMS experiment at the LHC*, Phys. Lett. B **716(1)**, 30 (2012)

[9] G. A. et al. (ATLAS), *Observation of a new particle in the search for the Standard Model Higgs boson with the ATLAS detector at the LHC*, Phys. Lett. B **716(1)**, 1 (2012)

[10] ATLAS, *ATLAS: technical proposal for a general-purpose pp experiment at the Large Hadron Collider at CERN*, Technical report, Geneva (1994), URL `https://cds.cern.ch/record/290968`

[11] G. B. et al., *Theory and phenomenology of two-Higgs-doublet models*, Phys. Rept. **516**, 1 (2012)

[12] M. Wikimedia, *Standard Model of Elementary Particles*, `https://upload.wikimedia.org/wikipedia/commons/0/00/Standard_Model_of_Elementary_Particles.svg`, [Online; accessed 23-Mar-2017]

[13] M. Kobayashi, T. Maskawa, *CP Violation in the Renormalizable Theory of Weak Interaction*, Prog. Theor. Phys. **49**, 652 (1973)

[14] N. Cabibbo, *Unitary Symmetry and Leptonic Decays*, Phys. Rev. Lett. **10**, 531 (1963)

[15] W. de Boer (CMS), *The Discovery of the Higgs Boson with the CMS Detector and its Implications for Supersymmetry and Cosmology*, in *Time and Matter 2013 (TAM2013) Venice, Italy* (2013), `1309.0721`, URL `https://inspirehep.net/record/1252561/files/arXiv:1309.0721.pdf`

[16] B. M. G. et al., *Report 4: Part I Standard Model Predictions*, Technical Report LHCHXSWG-DRAFT-INT-2016-008 (2016), URL `https://cds.cern.ch/record/2150771`

[17] M. de Souza, *Gravity cannot be quantized*, Technical Report gr-qc/0208085 (2002), URL `http://cds.cern.ch/record/578233`

[18] L. Wolfenstein, *Neutrino oscillations in matter*, Phys. Rev. D **17**, 2369 (1978)

[19] A. Sakharov, *Violation of Cp-Invariance C-Asymmetry and Baryon Asymmetry of the Universe*, Collected Works on Research into the Essentials of Theoretical Physics pages 84–87 (1998)

[20] G. Anderson, D. Castano, *Measures of fine tuning*, Phys. Lett. B **347(3-4)**, 300 (1995)

[21] E. Witten, *Mass hierarchies in supersymmetric theories*, Phys. Lett. B **105(4)**, 267 (1981)

[22] M. Thomson, *Modern particle physics*, Cambridge University Press (2013)

[23] R. Peccei, H. Quinn, CP *Conservation in the Presence of Pseudoparticles*, Phys. Rev. Lett. **38**, 1440 (1977)

[24] J. B. et al., *The measurement of the Higgs self-coupling at the LHC: theoretical status*, JHEP **04**, 151 (2013)

[25] D. de Florian Sabaris et al., *Handbook of LHC Higgs cross sections: 4. Deciphering the nature of the Higgs sector*, Technical Report LHCHXSWG-DRAFT-INT-2016-012 (2016), URL `https://cds.cern.ch/record/2215893`

[26] A. P. et al., *Disentangling dimension six operators through di-Higgs boson production*, JHEP **2007(05)**, 070 (2007)

[27] M. D. et al., *Higgs self-coupling measurements at the LHC*, JHEP **10**, 112 (2012)

[28] M. A. et al. (ATLAS), *Search for pair production of Higgs bosons in the $b\bar{b}b\bar{b}$ final state using proton–proton collisions at $\sqrt{s} = 13$ TeV with the ATLAS detector*, Phys. Rev. **D94(5)**, 052002 (2016)

[29] ATLAS, *Search for Higgs boson pair production in the final state of $\gamma\gamma WW^*(\rightarrow l\nu jj)$ using 13.3 fb^{-1} of pp collision data recorded at $\sqrt{s} = 13$ TeV with the ATLAS detector*, Technical report, CERN

[30] G. A. et al., *Searches for Higgs boson pair production in the $hh \rightarrow bb\ \tau\ \tau$, $\gamma\gamma WW^*$, $\gamma\gamma bb$, bbbb channels with the ATLAS detector*, Phys. Rev. D **92(9)**, 092004 (2015)

[31] O. B. et al., *LHC Design Report* (2004), URL `https://cds.cern.ch/record/782076`

[32] A. A. et al. (ATLAS), *ATLAS detector and physics performance : Technical Design Report, 1* (1999), URL `https://cds.cern.ch/record/391176`

[33] G. B. et al. (CMS), *CMS Physics : Technical Design Report* (2006), URL `https://cdsweb.cern.ch/record/922757/`

[34] R. A.-N. et al. (LHCb), *LHCb reoptimized detector design and performance : Technical Design Report* (2003), URL `http://cds.cern.ch/record/630827`

[35] F. P. et al. (ALICE), *ALICE high-momentum particle identification : Technical Design Report* (1998), URL `https://cds.cern.ch/record/381431`

[36] C. de Melis, *The CERN accelerator complex. Complexe des accelerateurs du CERN*, Technical Report OPEN-PHO-ACCEL-2016-001 (2016), general Photo, URL `https://cds.cern.ch/record/2119882`

[37] J. Pequenao, *Computer generated image of the whole ATLAS detector* (2008), URL `https://cds.cern.ch/record/1095924`

[38] N. Metropolis, S. Ulam, *The monte carlo method*, Journal of the American statistical association **44(247)**, 335 (1949)

[39] S. A. et al., *GEANT4 a simulation toolkit*, Nuclear instruments and methods in physics research section A: Accelerators, Spectrometers, Detectors and Associated Equipment **506(3)**, 250 (2003)

[40] W. Lukas, *Fast simulation for ATLAS: Atlfast-II and ISF*, in *Journal of Physics: Conference Series*, volume 396, IOP Publishing (2012)

[41] J. A. et al., *The automated computation of tree-level and next-to-leading order differential cross sections, and their matching to parton shower simulations*, JHEP **07**, 079 (2014)

[42] M. B. et al., *Herwig++ physics and manual*, The European Physical Journal C-Particles and Fields **58(4)**, 639 (2008)

[43] J. P. et al., *New generation of parton distributions with uncertainties from global QCD analysis*, JHEP **07**, 012 (2002)

[44] S. A. et al., *A general framework for implementing NLO calculations in shower Monte Carlo programs: the POWHEG BOX*, JHEP **2010(6)**, 1 (2010)

[45] T. S. et al., *A brief introduction to PYTHIA 8.1*, Computer Physics Communications **178(11)**, 852 (2008)

[46] H. L. et al., *New parton distributions for collider physics*, Phys. Rev. D **82(7)**, 074024 (2010)

[47] G. A. et al., *Measurement of the Z/γ^* boson transverse momentum distribution in pp collisions at s= 7 TeV with the ATLAS detector*, JHEP **2014(9)**, 1 (2014)

[48] R. B. et al., *Parton distributions with LHC data*, Nuclear Physics B **867(2)**, 244 (2013)

[49] *ATLAS Run 1 Pythia8 tunes*, Technical Report ATL-PHYS-PUB-2014-021, CERN, Geneva (2014), URL `https://cds.cern.ch/record/1966419`

[50] M. C. et al., *The anti-kt jet clustering algorithm*, JHEP **2008(04)**, 063 (2008)

[51] ATLAS, *Jet mass reconstruction with the ATLAS Detector in early Run 2 data*, Technical Report ATLAS-CONF-2016-035, CERN, Geneva (2016), URL `https://cds.cern.ch/record/2200211`

[52] G. A. et al. (ATLAS), *Jet energy measurement with the ATLAS detector in proton-proton collisions at* $\sqrt{s} = 7TeV$, The European Physical Journal C **73(3)**, 2304 (2013)

[53] ATLAS, *Jet energy measurement and its systematic uncertainty in proton–proton collisions at* $\sqrt{s} = 7$ *TeV with the ATLAS detector*, The European Physical Journal C **75(1)**, 17 (2015)

[54] ATLAS, *Measurement of large radius jet mass reconstruction performance at* $\sqrt{s} = 8$ *TeV using the ATLAS detector*, Technical Report ATLAS-CONF-2016-008, CERN, Geneva (2016), URL `https://cds.cern.ch/record/2139642`

[55] ATLAS, *Performance of jet substructure techniques for large-R jets in proton-proton collisions at* $\sqrt{s} = 7$ *TeV using the ATLAS detector*, JHEP **2013(9)**, 76 (2013)

[56] L. W. D. Krohn, J. Thaler, *Jet trimming*, JHEP **2010(2)**, 84 (2010)

[57] *Tagging and suppression of pileup jets with the ATLAS detector*, Technical Report ATLAS-CONF-2014-018, CERN, Geneva (2014), URL `https://cds.cern.ch/record/1700870`

[58] G. A. et al. (ATLAS), *Measurements of Higgs boson production and couplings in diboson final states with the ATLAS detector at the LHC*, Phys. Lett. **B726**, 88 (2013), [Erratum: Phys. Lett.B734,406(2014)]

[59] ATLAS, *Expected photon performance in the ATLAS experiment*, Technical Report ATL-PHYS-PUB-2011-007, CERN, Geneva (2011), URL `https://cds.cern.ch/record/1345329`

[60] ATLAS, *Electron efficiency measurements with the ATLAS detector using the 2015 LHC proton-proton collision data*, Technical Report ATLAS-CONF-2016-024, CERN, Geneva (2016), URL `https://cds.cern.ch/record/2157687`

[61] G. A. et al. (ATLAS), *Muon reconstruction performance of the ATLAS detector in proton–proton collision data at* $\sqrt{s}$*=13 TeV*, Eur. Phys. J. C **76**, 292. 45 p (2016)

[62] ATLAS, *Optimisation of the ATLAS b-tagging performance for the 2016 LHC Run*, Technical Report ATL-PHYS-PUB-2016-012, CERN, Geneva (2016), URL `http://cds.cern.ch/record/2160731`

[63] G. Cowan, E. Gross, *Discovery significance with statistical uncertainty in the background estimate*, ATLAS Statistics Forum (2008), URL `https://www.pp.rhul.ac.uk/cowan/stat/notes/SigCalcNote.pdf`

[64] V. K. et al. (CMS), *Search for a massive resonance decaying into a Higgs boson and a W or Z boson in hadronic final states in proton-proton collisions at* $\sqrt{s} = 8$ *TeV*, JHEP **02**, 145 (2016)

[65] P. Greenwood, M. Nikulin, *A guide to chi-squared testing*, volume 280, John Wiley & Sons (1996)

[66] ATLAS, *Jet Calibration and Systematic Uncertainties for Jets Reconstructed in the ATLAS Detector at* $\sqrt{s} = 13$ *TeV*, Technical Report ATL-PHYS-PUB-2015-015, CERN, Geneva (2015), URL `https://cds.cern.ch/record/2037613`

[67] C. A. et al., *Photon identification pre-recommendations for run 2*, Technical Report ATL-COM-PHYS-2015-496, CERN, Geneva (2015), URL `https://cds.cern.ch/record/2022342`

[68] ATLAS, *Measurement of Higgs boson production in the diphoton decay channel in pp collisions at center-of-mass energies of 7 and 8 TeV with the ATLAS detector*, Phys. Rev. D **90**, 112015 (2014)

[69] M. B. et al., *HistFitter software framework for statistical data analysis*, Eur. Phys. J. **C75**, 153 (2015)

Erklärung nach §17(9) der Prüfungsordnung für den Bachelor-Studiengang Physik und den Master-Studiengang Physik an der Universität Göttingen:

Hiermit erkläre ich, dass ich diese Abschlussarbeit selbständig verfasst habe, keine anderen als die angegebenen Quellen und Hilfsmittel benutzt habe und alle Stellen, die wörtlich oder sinngemäß aus veröffentlichten Schriften entnommen wurden, als solche kenntlich gemacht habe.
Darüberhinaus erkläre ich, dass diese Abschlussarbeit nicht, auch nicht auszugsweise, im Rahmen einer nichtbestandenen Prüfung an dieser oder einer anderen Hochschule eingereicht wurde.

Göttingen, den 4. November 2017

(Kai Henßen)